IONOSPHERIC PLASMA OUTFLOW IN RESPONSE TO TRANSVERSE ION HEATING

Semi-Annual Report

Grant: NAGW - 257 9

PI: Dr. N. Singh

During the last six months, we have investigated the transverse heating of H+ ions and the consequent dynamics of the polar wind. This work is reported in a recent paper [Singh, 1992]. A copy of the paper is enclosed. We have also examined the effect of transverse ion heating using a particle code. This work is in progress. Some initial results were presented in two papers at the last IUGG meeting in Vienna [Singh, 1991 a,b].

Singh, N., Electric Field Perturbations Created by Transverse Ion Heating Events, 20th General Assembly, IUGG, Vienna, August 11-24, 1991.

Singh, N., Plasma Perturbations Created by Transverse Ion Heating, 20th General Assembly, IUGG, Vienna, August 11-24, 1991.

Singh, N.,Plasma Perturbations Created by Transverse Ion Heating Events in the Magnetosphere, J. Geophys. Res., in press, 1992.

PLASMA PERTURBATIONS CREATED BY TRANSVERSE ION HEATING EVENTS IN THE MAGNETOSPHERE

NAGENDRA SINGH

Department of Electrical and Computer Engineering and Center for Space Plasma and Aeronomic Research
University of Alabama in Huntsville, Huntsville

Transversely heated ions provide an important mechanism for the transport of ionospheric ions to the distant parts of the magnetosphere. The heating occurs via wave-particle interactions. The transport of such ions has been generally treated by a test particle approach, according to which ions move upward adiabatically under the action of the mirror force. The perturbations in the plasma created by the heating are studied here for the first time by solving a self-consistent set of plasma transport equations, in which heating is included phenomenologically. The nature of the perturbation is found to depend on the field-aligned extent of the heating region and on the heating time. When the heating occurs in a relatively localized region, the perturbation consists of a density cavity topped by a density enhancement (bump). The plasma in the bump is that expelled from the cavity. For weak heating the bump propagates upward without any steepening near the density fronts. For relatively strong heating the bump steepens into a forward-reverse shock pair. The forward shock (F) forms near the leading edge while the reverse shock (R) is at the top of the density cavity, near the trailing edge of the bump. When the R-F shock pair has formed, the velocity profile shows double "sawtooth" structure. Such shock structures are similar to the features of interplanetary shocks associated with solar wind transients. Parallel temperatures of the ions are reduced inside the cavity and increased in the density bump adiabatically. The transversely heated ions occur inside the upper part of the cavity and in the density enhancement. The dynamics of the transversely heated ions is not determined by the mirror force alone. The electric fields developing in the perturbation significantly affect their upward motion; the electric fields near the lower edge (R) of the density bump are downward, and they retard the upward motion. The electric and mirror forces on the transversely heated ions are compared. The electric fields near the leading edge (F) of the density bump are upward, and when they are sufficiently strong they compress the ions in the ambient polar wind. This creates an ion population heated only in $T_\perp$ just near the leading edge of the perturbation. During the course of its evolution the electric field distribution shows pulselike features. For impulsive heating the distribution evolves into a predominantly unipolar upward pointing electric field near the leading edge. Such an electric field pulse moves upward and its field strength depends on the electron temperature and the density gradient across F. The perturbation produced by transverse heating extending over long distances is characterized by an upward expanding density cavity with its lower end anchored at the lower edge of the heating region. Inside the cavity the spatial distributions of density, flow velocity, and parallel and perpendicular temperatures reach a quasi-steady state while above it they continue to evolve. The dynamics of the ions in the cavity, including their pitch angle distribution, is described by a test particle approach under the influence of the mirror force. When the heating ceases, the cavity fills from the bottom through the expanding polar wind, and the transversely heated ions inside the cavity ride on top of this polar wind expansion.

1. INTRODUCTION

During the last decade, transversely heated ions have been extensively studied [e.g., *Klumpar*, 1986]. The transverse heating occurs by wave-particle interactions (see, for example, review by *Ashour-Abdalla and Okuda* [1983]). Both localized heating and extended heating have been studied in the literature. In the case of localized heating, the ions are heated in a region of limited extent, in which ions attain a pitch angle near 90°. As the ions move upward under the influence of the mirror force in the northern hemisphere, their pitch angle increases adiabatically [e.g., *Klumpar*, 1979]. When the heating is extended [*Temerin*, 1986], ion continually gain energy, and their pitch angle attains an asymptotic value [*Chang et al.*, 1986; *Singh and Hwang*, 1987]. The upward motion of the heated ions is generally considered by use of a simple test particle approach. The perturbations in the plasma created by the transverse heating, including its effect on the distributions of the plasma density, ion temperatures, and flow velocity, have not

been studied so far by solving a self-consistent set of plasma equations.

The purpose of this paper is to report our first attempt to understand the dynamics of the plasma perturbations created by transverse ion heating by solving an appropriate set of plasma transport equations similar to those for the polar wind. It is found that the heating-induced perturbations in the density, velocity, and temperature profiles of the ambient polar wind are quite severe. The temporal evolution of perturbations created by localized and by extended heating is presented here. For localized heating, the perturbation consists of a plasma cavity topped by a density bump which eventually evolves into a reverse-forward shock pair if the heating rate is sufficiently large. The parallel temperature structure in the perturbation is found to depend on the magnitude of the heat flow. Heat flow in a collisionless plasma is not a well-understood phenomenon. Therefore in the hydrodynamic model adopted in this paper, heat flows are included phenomenologically. Anomalous plasma effects may severely inhibit the heat flux [*Manheimer*, 1977]. The parallel temperature distributions for different heat flow conditions are presented.

The density cavity and the bump are the results of the expulsion of the heated ions by the mirror force. Thus it is expected that the ions in the entire bump be transversely heated. This is found to be true only initially. As the bump evolves, its leading edge compresses the ambient polar wind as a snowplow compresses snow ahead of it. This newly compressed plasma becomes part of the bump, but it is heated only in $T_{\parallel}$. Consequently, the transversely heated ions are found near the top of the cavity and in the lower part of the density bump, and not near its leading edge. However, the exact topology of the ions with enhanced $T_{\parallel}$ and/or $T_{\perp}$ depends on several factors, such as the heating time and the electron temperature.

The electric field distributions associated with the perturbations in the plasma flow show pulselike features. The electric fields in the pulses can point downward or upward depending on their location with respect to the density bump. When heating is very brief in time and localized in space, the evolving perturbation has an electric field distribution dominated by an upward pointing electric field pulse near its leading edge. Such fields appear as upward moving weak double layers.

Electric fields developing inside the perturbations are found to have significant effects on the upward motion of the transversely heated ions. Just before the reverse shock forms, the downward electric field force near the trailing edge of the bump exceeds the mirror force on the ions. At later times the two forces are found to be comparable. Thus the upward motion of the transversely heated ions is determined not by the mirror force alone, but by the self-consistent evolution of the entire perturbation.

When the heating is extended, the major feature of the perturbation is the formation of a deep plasma cavity topped by an extended density enhancement, which is relatively weak. The cavity progressively expands upward. Inside the density cavity the flow reaches a quasi-steady state which is maintained as long as the heating lasts. The relaxation of the polar wind after the heating ceases is presented.

Previously, time-dependent polar wind studies have been carried out by several authors: *Singh and Schunk* [1985] studied the evolution of reverse and forward shock pairs when the polar wind was artificially disturbed by density cavities and bumps. The present study shows how such cavities and bumps are naturally created by transverse ion heating. *Gombosi and Killeen* [1987] studied transients in response to low-altitude ion heating. *Mitchell and Palmadesso* [1983] and *Ganguli and Palmadesso* [1987] have studied the time-dependent features of the polar wind in response to the wave-particle interactions driven by field-aligned currents. The latter authors have dealt with the issue of transverse ion heating, but the features of the perturbations in response to transverse heating of the polar wind, as seen in the present paper, have not been reported.

The rest of the paper is organized as follows; in section 2 the theoretical model is described. The results of the perturbation and its evolution are described in section 3, which includes discussions of the effects of heating rate, heating time interval, heating region size, electron temperature, and heat flow on the evolution. The paper is concluded in section 4.

2. THEORETICAL MODEL

We model here the transport of plasma in response to the transverse heating of the polar wind at altitudes of ≥3000 km. The relevant equations governing the magnetic-field-aligned transport of the mass, momentum, and thermal energies of hydrogen ions in a collisionless plasma are given by

$$\frac{\partial n_i}{\partial t} + \frac{\partial}{\partial s}(n_i V_i) = -n_i V_i \frac{1}{A}\frac{\partial A}{\partial s} \tag{1}$$

$$\frac{\partial V_i}{\partial t} + \frac{\partial}{\partial s}\left(\frac{1}{2}V_i V_i\right) = (e_i/m_i)E - (k_B/m_i)\frac{\partial T_{\parallel i}}{\partial s} - (k_B/m_i)T_{\parallel i}\frac{1}{n_i}\frac{\partial n_i}{\partial s}$$

$$- g_{\parallel}(r) - (k_B/m_i)(T_{\parallel i} - T_{\perp i})\frac{1}{A}\frac{\partial A}{\partial s} \tag{2}$$

$$\frac{\partial T_{\parallel i}}{\partial t} + \frac{\partial}{\partial s}(V_i T_{\parallel i}) = -T_{\parallel i}\frac{\partial V_i}{\partial s} - \frac{1}{n_i}\frac{1}{A}\frac{\partial}{\partial s}(q_{\parallel i}A) \tag{3}$$

$$\frac{\partial T_{\perp i}}{\partial t} + \frac{\partial}{\partial s}(V_i T_{\perp i}) = T_{\perp i}\frac{\partial V_i}{\partial s} - T_{\perp i}V_i\frac{1}{A}\frac{\partial A}{\partial s}$$

$$- \frac{1}{n_i}\frac{1}{A}\frac{\partial}{\partial s}(q_{\perp i}A) + \left(\frac{\partial T_{\perp}}{\partial t}\right)_{\text{turb}} \tag{4}$$

where t is time; r is the geocentric distance along the flux tube; s is the distance along the tube from the lower boundary of the flux tube at $r = r_o$ (see Figure 1); n_i, V_i, $T_{\parallel i}$, and $T_{\perp i}$ are the number density, flow velocity, and parallel and perpendicular temperatures of the polar wind, respectively; E is the parallel electric field; $g_{\parallel}$ is the component of the gravitational force parallel to the magnetic field; and m_i and q_i are the ion mass and charge, respectively. A is the cross-sectional area of a flux tube, and it is assumed that $A \propto r^3$. Except for the time-independent terms, equations (1) to (4) are similar to the formulation given by *Holzer et al.* [1971], who derived these

equations directly from the moments of the Boltzmann equation. We do not solve the heat flow equations, which have proven to be quite troublesome to solve numerically [*Palmadesso et al.*, 1988]. Instead, we have included the effects of heat flow heuristically by closely following the treatments in solar wind studies [e.g., *Metzler et al.*, 1979].

In a collisionless plasma the usual picture of heat flow, given by $q_\alpha = -K_\alpha \nabla T_\alpha$ with K_α as the thermal conductivity, may not be valid because λ, the mean free path, is $>> L_T = (T^{-1} \partial T/\partial s)^{-1}$, the scale length in the temperature variation. In such a situation, maximum heat flux is given by the transport of the thermal energy density ($nk_B T_\alpha$) by the parallel thermal velocity $V_{th} = (k_B T_\parallel/m_i)^{1/2}$, where T_α denotes $T_\perp$ or $T_\parallel$. However, plasma turbulence has been found to inhibit the heat flow drastically [*Manheimer*, 1977]. Accordingly, we assume that

$$q_{\alpha i} = \epsilon \eta n_i k T_{\alpha i} V_{th} \tag{5}$$

where $\epsilon = -1$ if $\partial T_\alpha/\partial s > 0$ and $\epsilon = 1$ if $\partial T_\alpha/\partial s < 0$. Thus temperature gradients determine only the sign of the heat flow and not its magnitude. The factor η is the reduction due to the anomalous plasma effects. In the present macroscopic calculations we cannot determine the value of η self-consistently. Therefore, in order to develop a feel for the effects of heat flow, calculations are performed by varying η from 0.01 to 1.

The electric field E is obtained from the electron momentum equation by making the following assumptions: (1) plasma remains quasi-neutral, $n_e = n_i$; (2) electron temperature ($T_e(s)$) is isotropic and does not vary with time during the evolution of the plasma perturbation; and (3) electron flow velocity is calculated from the condition of no field-aligned current, i.e., $n_e V_e = n_i V_i$ or $V_e = V_i$ when $n_i = n_e$. Thus the electric field is given by

$$E = -\frac{1}{e}\left[m_e \frac{\partial V_i}{\partial t} + \frac{\partial}{\partial s}\left(\frac{1}{2} m_e V_e^2\right) + \frac{1}{n_e} \frac{\partial (n_e k T_e)}{\partial s}\right] \tag{6}$$

In the calculations presented here, we have limited the perpendicular ion heating to a relatively low level, for which it is found that the first two terms in equation (6) make negligibly small contributions to E. Since we do not solve the electron energy equation, care has been exercised to ensure that the spatial variation in the flow velocity has a negligible effect on the electron temperature. This is possible when the electron thermal velocity is considerably greater than the flow velocity. Calculations are presented with both constant and variable electron temperatures with altitude.

It is likely that the electrons may develop a temperature anisotropy [*Mitchell and Palmadesso*, 1983]; its contribution to the electric field is proportional to $3/r$, where r is the geocentric distance; inside the perturbation where the density and/or velocity have relatively large gradients, this contribution by the electron temperature anisotropy is found to be negligibly small compared to the third term in equation (6), unless the perpendicular electron temperature becomes comparable to the perpendicular temperature of the heated ions. Further quantitative comparison between the various contributions to E will be given later in the paper.

Equations (1) to (4) are written in the form of a generalized continuity equation and are solved numerically by the flux-corrected transport technique [*Boris and Book*, 1976]. These equations are solved as an initial boundary value problem. The initial conditions correspond to the steady state (ambient) polar wind, in which protons flow supersonically. The boundary conditions are as follows; at the lower boundary ($r = r_o$) we assume that $n = N_o$, $V = V_o$, and $T_\perp = T_\parallel = T_o$, where N_o, V_o, and T_o are the ionospheric density, flow velocity, and temperature at the altitude $r = r_o$. In the present calculation it is assumed that $N_o = 500$ cm^{-3}, $T_o = 0.3$ eV, and the value of V_o is varied from case to case depending on the electron temperature T_e, which exercises a great deal of control on the flow velocity. At the top boundary ($r = r_{max}$) the continuity of the flow is maintained.

The heating rate $\delta T_\perp/\delta t$ appearing in (4) is given by

$$(\delta T_\perp/\delta t)_{turb} = 0.25\,(q_i^2/m_i)\psi \qquad (7)$$

where ψ is the wave power spectral density in units of V^2 m^{-2} Hz^{-1}. Such a heating rate is the consequence of the interaction of ions with broadband waves when the wavelengths are much larger than the ion Larmor radius [*Singh and Schunk*, 1984; *Chang et al.*, 1986]. It is worth mentioning that knowledge of the exact nature of the heating is not important here, as we are studying the large-scale effect of the heating on the polar wind rather than the microscopic causes of the heating. In the calculations presented here, different values of ψ are adopted depending on the desired heating level.

3. PLASMA PERTURBATION

We present here the nature of the plasma perturbation created by the transverse heating of the ions. The temporal evolution of the spatial structure of perturbations for different heating rates, size of the heating region, and electron temperature distributions is discussed.

3.1. *Localized Heating*

It is instructive to examine the nature of the perturbations for a relatively low heating rate, which produces relatively weak perturbations. Figures 2*a* to 2*d* show the evolution of the perturbation when the heating occurs over a distance $\Delta s_h = 210$ km starting at a height of 5100 km ($s = 2100$ km). The heating rate is 0.24 eV/s, which is obtained from (7) for a power spectral density $\psi = 10^{-8}$ V^2 m^{-2} Hz^{-1}. The heating time interval Δt_h is 1.844 min. The electron temperature distribution is assumed to be a constant, $T_e(s) = 1$ eV. The heat flow reduction parameter η is 0.5. Figures 2*a* to 2*d* show the evolution of density, flow velocity, parallel temperature, and perpendicular temperature, respectively. The profiles shown in this figure are at times t_0, t_1, t_2, t_4, and t_6 where $t_n = n \times 0.922$ min. The profiles at $t = t_o$ correspond to the initial unperturbed polar wind. The perturbations in n, V, and $T_\parallel$ are minimal at $t_1 = 0.922$ min as they are hardly visible at the scales used in the figures. However, at this time the perturbation in $T_\perp$ indicates a heating up to a maximum value of ~3 eV. Eventually, the perpendicular heating affects other quantities, and the perturbations in n, V, and $T_\parallel$ can be clearly seen for $t \geq t_2$.

The perturbation in the density consists of a cavity topped by a density enhancement. This perturbation is simply the consequence of the expulsion of the plasma by the mirror force acting in the region with enhanced $T_\perp$. The density perturbation is accompanied by an enhancement in the flow velocity (Figure 2*b*) and by a reduction in the parallel temperature inside the plasma cavity and an increase inside the density enhancement. The structure in the parallel temperature is accounted for by an adiabatic expansion inside the cavity and a compression inside the density enhancement [e.g., *Tanenbaum*, 1967]. For example, the minimum parallel temperature ($T_{\parallel min}$) in the plasma cavity and the maximum temperature ($T_{\parallel max}$) in the density enhancement are found to approximately obey the relation

$$T_{\parallel min}/T_{\parallel max} = (n_{min}/n_{max})^2 \qquad (8)$$

which comes from the adiabatic law $T_\parallel n^{1-\gamma} = \text{const}$ with $\gamma = 3$ for a one-dimensional process.

Figures 2*a* to 2*d* show that as long as the heating continues the lower end of the perturbation remains fixed at the altitude of the lower edge of the heating region. This is seen very clearly by comparing the profiles at $t = t_1$ and t_2 in Figure 2*d*. When the heating stops, the entire perturbation moves upward. The upward moving perturbation rides on the upward flowing polar wind. The peak in the density enhancement is seen to move with a velocity $V_{pert} \approx 14$ km/s, which is considerably slower than the flow velocities inside the perturbation. As the transversely heated ions move upward after the heating stops, the maximum value of $T_\perp$ continually decreases. This decrease is found to be approximately adiabatic, i.e., $T_{\perp max} \propto B$.

Enhanced heating rate. When the heating rate is enhanced, the evolution of the plasma perturbation is seen to change considerably. Figures 3*a* to 3*d* show the evolution of the perturbation when the heating rate ($\partial T_\perp/\partial t$) is 2.4 eV/s, in contrast to 0.24 eV/s for the perturbation shown in Figures 2*a* to 2*d*. All other parameters for Figures 3*a* to 3*d* are the same as for Figures 2*a* to 2*d*. When $t = t_1 = 0.922$ min, the transverse heating has increased $T_\perp$ to a maximum value $T_{max} = 30$ eV (Figure 3*d*), which is about 10 times the maximum $T_\perp$ at $t = t_1$ in Figure 2*d*. As in Figures 2*a* to 2*c*, Figures 3*a* to 3*c* show the formation of a plasma cavity topped by a density bump, enhancement in the flow velocity throughout the plasma perturbation, a decrease in the parallel temperature in the cavity, and an increase in the bump. However, there are significant differences between the magnitudes of the perturbations shown in Figures 2*a* to 2*d* and Figures 3*a* to 3*d*. Consequently they evolve quite differently.

The large-amplitude perturbations in density and velocity profiles produce nonlinear effects. A prominent effect of nonlinearity is that the leading edges of the perturbations in Figures 3*a* to 3*c* are relatively much steeper than those seen in Figures 2*a* to 2*c*. This is a common feature of the nonlinear evolution of ion acoustic shocks and solitary waves [*Tidman and Krall*, 1971].

The leading edge of the perturbation indicated by F in Figures 3*a* to 3*c* is a forward shock, which connects the perturbation with the ambient polar wind. The forward shock (V_{fs}) velocity is calculated by the conservation of mass flow by

the relation

$$V_{fs} = \frac{n_1 V_1 - n_a V_a}{n_1 + n_a} \tag{9}$$

where n_1 and V_1 are the peak density and velocity, respectively, near the forward shock F and n_a and V_a are the corresponding quantities of the ambient polar wind just above the shock. At $t = t_6$, $n_1 = 0.178\ n_o$, $V_1 = 48$ km/s, $n_a = 0.047\ n_o$, and $V_a = 29$ km/s, giving $V_{fs} = 32$ km/s, which is found to be in agreement with the shock velocity calculated from the time of flight; the shock positions at $t = t_5$ and t_6 are at $s = 7560$ km and $s = 9240$ km, respectively, giving $V_{fs} = 31$ km/s. This agreement indicates that the shock is quite steady as it moves upward.

There is an interesting process which occurs near the leading edge (F). The perturbation in parallel temperature runs slightly ahead of that in the perpendicular temperature. This is shown by the dashed vertical line running through all four panels of Figure 3. On the right-hand side of this line the ions in the density enhancement are not heated in $T_\perp$; instead, they are heated in $T_\parallel$ up to about 2 eV. It is worthwhile to understand the origin of such ions in the perturbation. Initially, when the transverse heating produces a perturbation in the form of a density enhancement by expelling plasma via the mirror force, the entire plasma in the perturbation is heated in $T_\perp$. For relatively strong heating, as shown in Figure 3, the density enhancement is strong. The upward electric field and the pressure forces near the leading edge (F) are able to further compress the plasma in the ambient polar wind just ahead of the perturbation produced by the mirror force. The newly compressed plasma is not heated in $T_\perp$, but the adiabatic compression leads to the enhancement in $T_\parallel$. As will be shown later, this effect is considerably enhanced when an increase in the electron temperature enhances the electric field near F (see Figure 10). This process of ion heating has been seen previously in plasma expansion studies [*Mason*, 1971; *Singh and Schunk*, 1983], and more recently it has been termed an electrostatic "snowplow" [*Schunk and Szuszczewicz*, 1988].

Just like the pressure and electric forces near the leading edge, the downward forces near the trailing edge of the density enhancement significantly affect the evolution of the perturbation. In particular, such forces lead to the formation of a reverse shock (R) near the trailing edge of the density bump. At an early time ($t < t_2$) the velocity profile (Figure 3*b*) has only one "sawtooth" distribution. At later times ($t > t_4$) it develops two sawtooth distributions, one near the leading edge (F) and the other near the trailing edge. The latter sawtooth distribution begins to form at about $t = t_4$. This sawtooth formation proceeds as follows. When the downward electric and pressure forces associated with the sharp gradients near the trailing edge of the density bump become strong enough, the flow is slowed down there. Such local slowing down of the flow leads to the formation of the new sawtooth in the flow velocity.

The structure in the flow near the new sawtooth is a reverse shock (R), where the upward jumps in the density and $T_\parallel$ are accompanied by a downward jump in the velocity. In contrast to this both velocity and density jumps are downward across the forward shock.

Reverse shocks are known to form in a variety of situations, such as the transient solar wind [*Hundhausen*, 1973] and some types of nozzle flows [*Liepmann and Roshko*, 1957]. The physical factor facilitating the formation of a reverse shock is the creation of a low-pressure zone in a high-speed flow. Transverse heating produces such a situation when the plasma is evacuated by the mirror force. However, it is important to note that only when the heating and the associated perturbations in the plasma are strong enough, do the reverse and forward shocks form. This point is well illustrated by comparing the results in Figures 2*a* to 2*d* with those in Figures 3*a* to 3*d*, which are for weak and strong heating, respectively.

The evolution of the electric fields during the evolution of the plasma perturbation is shown in Figure 4. The electric fields are primarily determined by the slopes in the density ($\partial n/\partial s$ term in equation (6)) profiles. The time variation of the velocity V_i and the slopes in its profile do not significantly contribute to the fields. The solid curve in Figure 4 is the contribution by $\partial n/\partial s$ alone while the circles show the sum of the contributions of all three terms in equation (6) for the electric field. It is clearly seen that the two curves are remarkably close, implying that the contributions from the terms containing $\partial V/\partial t$ and $\partial V/\partial s$ in equation (6) are insignificant.

The role of the downward electric field in the formation of the reverse shock can be appreciated by noting that at $t = t_4$ a large downward (negative) electric field develops. The maximum value of the negative electric field is about -9 μV/m. This field plays a crucial role in slowing down the flow and thereby in the formation of the sawtooth "R," where the reverse shock forms. In order to clearly demonstrate this point, we have compared in Figure 5 the mirror force on the ions with the electric force arising from the electric fields associated with the perturbations. The mirror force F_m is calculated using

$$F_m = e\,\frac{3T_{\perp i}}{r} \qquad (10)$$

where $T_{\perp i}$ is in electron volts and r is the geocentric distance. The solid and dashed curves in Figure 5 show the electric field and F_m/e in units of microvolts per meter, respectively. We note that at $t \le t_2$, F_m exceeds the downward electric force eE almost over the entire perturbation. However, at $t = t_4$ the maximum downward electric field is 9 μV/m while at the same location the upward mirror force per unit charge is $\le$4 μV/m. The excess of the downward electric force locally slows the transversely heated ions forming the sawtooth in V at R. At later times this trend is continued as $T_\perp$ decreases with increasing altitude.

Effects of heating duration. It is certain that the transverse heating events in space occur over a variety of temporal and spatial scales. Here we discuss the nature of the perturbation when the heating time interval (Δt_h) is reduced while the heating rate is enhanced to achieve a desired heating level. Figure 6 shows results for Δt_h = 0.1844 min and $(\partial T_\perp/\partial t)_{turb}$ ~ 24 eV/s, while Δs_h = 210 km and η = 0.5 as in Figures 2 and 3. The basic nature of the perturbation in this figure is the same as in Figure 3. However, there is a difference in its evolution. We noted earlier while discussing Figures 2 and 3

that the lower end of the perturbations remains fixed as long as the heating is on. When the heating is over, the composite perturbation moves upward, riding on top of the ambient polar wind expanding upward. Since the heating time is 0.1844 min in Figure 6 in contrast to 1.844 min in Figure 3, the composite perturbation begins to ride on top of the upward expanding polar wind earlier in Figure 6 than in Figure 3. Consequently, the shorter the heating event, the higher the perturbation moves upward. Comparing Figures 3*a* and 6*a*, we find that in the latter figure the leading edge of the perturbation has reached the distance s = 12,000 km in contrast to 10,000 km in Figure 3.

Effect of heat flow on the perturbation. In the above discussion we assumed that the heat flow reduction factor η is 0.5 in equation (5). Since the value of η is uncertain, it is worthwhile to carry out a parametric study that varies η to see how the variation affects the evolution of the plasma perturbation. Figure 7 shows the comparison of the perturbations for η = 0.01 (dashed curves) and η = 1 (solid curves), respectively. The panels in the left- and right-hand columns show the perturbation at early and late times, respectively. The choice of η = 0.01 implies a negligibly small heat flow. On the other hand, η = 1 yields the maximum heat flow. The early time perturbation in the left-hand column clearly demonstrates that the heat flow has negligibly small effect on the density and flow velocity while temperature profiles are slightly modified. On the other hand, at relatively late times when the reverse shock has formed, even the density and flow velocity profiles show significant modification by the enhanced heat flow. The most significant effects in the $n(s)$ and $V(s)$ profiles are found near the reverse shock, where flow velocity is relatively reduced. With reduced flow velocity the transport of the thermal energy due to the thermal motion becomes more important. The enhanced heat flow is seen to stretch out the region of enhanced parallel and perpendicular temperature. The density depletion and the reduction in the parallel temperatures in the plasma cavity are less severe with the enhanced heat flow.

The heat flow also has significant effects on the propagation of the reverse and forward shock pair. The forward shock is seen to move faster with increasing heat flow. On the other hand, the reverse shock slows down. Consequently, the density enhancement and the associated features in $T_\parallel$ and velocity distributions are stretched out. However, it must be said that the basic features of the perturbations created by the transverse ion heating are not severely affected by the heat flow. This is true at least for the time span over which the evolution for η = 0.01 and 1 is shown.

Effect of increasing electron temperature with altitude. In the calculations presented so far, electron temperature T_e was assumed to be constant all along the flux tube. Since electrons are expected to be progressively warmer with increasing altitude, it is useful to examine the effects of such electron temperature distributions on the evolution of the plasma perturbations. Not knowing an exact distribution, we have arbitrarily chosen here that the electron temperature linearly increases from 0.3 eV at s = 0 to 5 eV at s = 16,500 km. The choice of the temperature at the high altitude is guided by observations that at altitudes of about 1 R_E the thermal

electron temperature can be up to several electron volts [e.g., *Kintner et al.*, 1979].

Figures 8 and 9 show the evolution of the plasma perturbations for this electron temperature distribution. Other parameters for the calculations shown in these figures are the same as those for Figures 3 and 4. The basic features of the perturbation, namely, the formation of a plasma cavity topped by a density enhancement and its eventual evolution into a reverse-forward shock pair, are similar to those in Figures 3*a* to 3*d*. So is the evolution of electric field perturbations for the two sets of calculations with a constant electron temperature of 1 eV (Figure 4) and with the electron temperature increasing with altitude (Figure 9). However, there are some interesting quantitative differences. For the assumed electron temperature distribution in Figure 8, $T_e(s) > 1$-eV for the entire perturbation in contrast to a constant 1 eV temperature over the entire perturbation shown in Figure 3. Thus, wherever a sharp density gradient develops in the perturbation, the magnitude of the electric field becomes larger for the perturbation in Figure 8 than for the perturbation in Figure 3. For example, at $t = t_2$, the electric field (Figure 9*b*) near the trailing edge of the density bump (Figure 8*a*) is nearly twice the corresponding electric field (Figure 4*b*) with the constant 1-eV value of T_e. This hastens the formation of the reverse shock near the trailing edge in Figure 8. Since the reverse shock moves slower than the forward shock, the density bump (Figure 8*a*) and the associated enhancement in the parallel temperature (Figure 8*c*) are considerably stretched out. This stretching of the perturbation can be clearly seen by comparing the electric field distributions at $t = t_6$ in Figures 4*d* and 9*d*.

The electric field enhancement near relatively large density gradients caused by an increase in the electron temperature is found to affect the upward motion of the transversely heated ions. For example, Figure 8*d* shows that at $t = t_6 = 5.6$ min, transversely heated ions have traveled upward to a height $s \approx$ 8200 km in contrast to a considerably greater height of 9300 km in Figure 3*d*, in which the electron temperature has a constant value of 1 eV. The heights quoted here are for the locations at which $T_\perp(s)$ suddenly begins to fall with increasing altitude. This retardation of the transversely heated ions is a direct consequence of the enhancement of electric fields due to enhanced electron temperature. As mentioned earlier, the downward electric fields retard the motion of the upward moving ions. The downward fields in Figure 9 are found to be consistently higher than those in Figure 3.

Perturbations associated with impulsive ion heating. In the previous examples of ion heating, the heating was relatively extended over a distance of $\Delta s_h = 210$ km. We now wish to examine the nature of the perturbation when the size of the heating region is reduced. In the example presented here we assume $\Delta s_h = 60$ km. Owing to numerical constraints we are not able to further reduce Δs_h and at the same time follow an extended length of the flux tube to allow for the evolution of the perturbation. Along with the size Δs_h, the heating time Δt_h is also reduced to 5 s. Thus the heating simulated in this example is quite impulsive in both time and space. In order to have a substantial perpendicular heating for the limited values of Δs_h and Δt_h, the heating rate is enhanced to 240 eV/s, which corresponds to $\psi = 10^{-5}$ V^2 m^{-2} Hz^{-1} in equation (7). We

have assumed here that electron temperature T_e is 10 eV over the entire region of the perturbation and that $\eta = 0.5$.

Figures 10*a* to 10*d* show the evolution of the perturbations up to $t = t_4 = 2$ min. Note that $t_n = n \times 30$ s in this figure. As in previous examples, we find that at an early time ($t \leq t_1$) the basic feature of the perturbation is the formation of a plasma cavity topped by a density enhancement. However, at later times the evolution differs from the previous example in a significant way concerning the formation of the reverse shock. The density and velocity profiles show that the reverse shock does not develop fully. The sawtooth in the velocity profile near the trailing edge of the bump remains weak all along the evolution shown in Figure 10*b*. It is seen that the leading edge (F) of the density bump is quite steep, but its trailing edge is seen to smooth out with increasing time. This is attributed to the fact that in the impulsive heating lasting over a short duration, the cavity begins to refill from the bottom at an early stage through the upward expansion of the polar wind. Thus the pressure inside the cavity does not become low enough for the reverse shock to develop fully. The forward shock and its dynamics are found to be quite similar to those in the previous case as discussed in connection with Figure 3.

The electric field perturbations for the impulsive heating are shown in Figures 10*e* to 10*h*. The most noteworthy feature of the electric field distribution shown in this figure is its evolution to a predominantly unipolar upward pointing electric field near the leading edge of the density bump when $t \geq t_2 \sim 1$ min. This dominant electric field pulse propagates upward with a velocity of about 60 km/s, which is about twice the H^+ ion acoustic speed with 10-eV electrons. Such upward propagating electric field pulses appear quite similar to the predominantly unipolar electric fields observed in the auroral plasma [*Temerin et al.*, 1982]. However, the observed fields are generally interpreted as ion acoustic double layers which have scale lengths of a few tens of Debye lengths (≤100 m). In contrast, in the present calculations we have a spatial resolution of ~60 km, which is the minimum intergrid spacing used in our calculations. Therefore, if there is any connection between the observed electric field pulses and those pulses generated by impulsive ion heating presented in this paper, it remains to be explored. Observationally, this task requires a close scrutiny of the plasma data along with the data on electric fields, correlating the perturbation in the plasma density with the electric field pulses. Theoretically, it is essential that the temporal and spatial scales of the calculations be reduced to the extent that the electronic field pulses of durations of a few milliseconds be produced. As mentioned earlier, such temporal resolution becomes extremely demanding in terms of computer resources. Therefore the main point of the discussion here is to suggest that perpendicular ion heating can produce parallel electric fields. We cannot rigorously compare such fields with double layers.

Figures 10*a* to 10*c* again show that the leading edge of the perturbation travels ahead of the transversely heated ions. As discussed earlier, the primary reason for this behavior is that the large electric field near the leading edge acts like an electrostatic "snowplow" compressing the plasma just ahead of it. This compressed plasma ahead of the transversely heated ions has enhanced $T_\parallel$ but not $T_\perp$. This is clearly seen from Figures 10*c* and 10*d*. As in Figure 3, the dashed vertical line

separates this compressed plasma from the transversely heated ions.

3.2. *Extended Heating Events*

A role of extended transverse heating of ions in producing ion conics having nearly constant cone angles with variation in the geomagnetic latitude has been suggested in explaining observations from the ISEE 1 satellite of low-energy ion conics in the outer region of the plasmasphere [*Horwitz et al.*, 1982; Singh, unpublished manuscript, 1980]. More recently, extended ion heating has been proposed as a mechanism for producing ion conics in the auroral plasma [*Temerin*, 1986], in the plasma sheet [*Chang et al.*, 1986], and in the refilling zone of the outer plasmasphere [*Singh and Hwang*, 1987]. However, all these studies have been essentially based on a test particle approach, in which the plasma perturbation is ignored. We discuss here the nature of the plasma perturbation produced by transverse ion heating occurring over an extended region along an open flux tube. Figures 11*a* to 11*d* show the evolution of the perturbations in density, velocity, parallel temperature, and perpendicular temperature profiles, respectively, in response to an extended heating event. The perturbations shown in this figure are for a relatively low heating rate of 0.24 eV/s above the distance $s = s_o = 6000$ km (altitude 9000 km). The electron temperature is assumed to be 1 eV all along the flux tube. We assumed that $\eta = 0.5$. Qualitatively similar results were obtained when T_e was allowed to vary with altitude according to $T_e(s) = 0.3$ eV + 4.3×10^{-5} s eV/km, which yields a temperature of 0.3 eV at the boundary $s = 0$ and 2.5 eV at the top of the flux tube considered in the calculations (Figure 1). In Figure 11, $t_n = n \times 1.844$ min. The evolution of the density profile (Figure 11*a*) shows that the primary effect of the heating is the evacuation of plasma beginning at $s = s_o$. The plasma cavity formed by the evacuation continually expands upward. The expansion velocity of the cavity front after the initial stage ($t \geq t_3$) is found to reach an asymptotic value of 50 km/s.

Figure 11*a* shows that density above the expanding cavity increases only slightly in comparison to the increase in the density enhancements for localized heating. This is primarily due to the continual upward acceleration of the ions by the mirror force resulting from continual transverse heating in space. Acceleration of ions resulting in a velocity increment above the cavity can be seen from Figure 11*b*. It is found that at any given time the velocity and density profiles reach quasi-steady states below the leading edge of the cavity. Above the leading edge of the density cavity the flow velocity is still evolving through the acceleration of ions by the mirror force. Inside the cavity, where the steady state is reached, the mirror force is found to balance the nonlinear $\partial/\partial s(1/2\ V^2)$ term in the momentum equation, i.e.,

$$\frac{\partial}{\partial s}\left(\frac{1}{2}(mV_i^2)\right) = k_B T_{\perp i} \frac{1}{A}\frac{\partial A}{\partial s} = \frac{3}{r} k_B T_{\perp i}(r) \qquad (11)$$

In order to demonstrate this force balance we compared the ion flow velocity obtained by integrating the above equation with the velocity profiles shown in Figure 11*b*. $T_{\perp i}(r)$ used in the integration are the same as in Figure 11*d*. At any time the

integration is carried out from bottom to top of the cavity. The comparison is shown in Figure 12. The dashed curves in Figures 12*a* to 12*d* are the product of integrating (11), while solid curves are the same as in Figure 11*b*. It is seen that equation (11) predicts the flow velocity inside the cavity quite accurately. In view of this close agreement, it is interesting to note that during the steady state phase the fluid flow is essentially given by the test particle approach. In this situation the pressure and electric forces are dominated by the mirror force. However, this is true only if the transverse heating results in relatively large perpendicular temperatures.

The evolution of the parallel temperature (Figure 11*c*) shows that ions cool down inside the cavity while they are slightly heated above it as the plasma is compressed to a slightly higher density. Figure 11*d* shows that as the ions enter the heating region they quickly acquire a relatively large perpendicular temperature. This results in parallel acceleration of ions through the mirror force. Therefore, as ions move up, their transit time through a given distance in space continually decreases. This leads to a continually decreasing spatial increment in $T_\perp$, despite a constant heating rate with respect to time. This feature is borne out from Figure 11*d*. The log scale used in Figure 11*d* does not allow one to clearly see the evolution of $T_\perp(s)$. Therefore $T_\perp(s)$ is replotted in Figure 13. It is seen that after the cavity forms at $t \geq t_3 = 5.5$ min, $T_\perp$ is lower inside the cavity than above it. Inside the cavity, $T_\perp(s)$ attains a quasi-steady profile as $n(s)$, $V(s)$, and $T_\parallel(S)$ do.

It is useful to examine the spatial evolution of the ion pitch angle defined by

$$\tan \alpha_p = \left(\frac{2k_B T_{\perp i}}{m_i} \right)^{1/2} / V_i \tag{12}$$

where V_i is the parallel flow velocity. Figure 14 shows the distribution of $\alpha_p(s)$ at $t = t_9$, when the leading edge of the density cavity shown in Figure 11*a* is just about to exit from the top of the calculation region which extends up to $s = 52{,}500$ km. As expected, below the heating region, α_p is found to steadily decrease with increasing height. Near the lower edge of the heating region, α_p abruptly attains a large value over a relatively short distance of about 2000 km. The maximum pitch angle is about 63° (or 117° in the northern hemisphere). Then it steadily decreases and asymptotically reaches 30°. This asymptotic value of the pitch angle can be analytically estimated as follows. Using a test particle approach, the motion of an ion through the heating region is described by [*Singh and Hwang*, 1987]

$$\frac{\partial W}{\partial r} = k_B (\partial T_\perp / \partial t)_{\text{turb}} V_i^{-1} \tag{13}$$

$$W \frac{d\alpha_p}{dr} = \sin^{-1}\alpha_p \left[-\frac{3W}{r} \sin^2\alpha_p + k_B \left(\frac{\partial T_\perp}{\partial t} \right)_{\text{turb}} V_i^{-1} \cos^2\alpha_p \right] \tag{14}$$

where $W = \frac{1}{2} m V_i^2 + 2k_B T_\perp$. When α_p tends to its asymptotic value, $d\alpha_p/dr = 0$, yielding

$$\tan^2\alpha_p = \frac{r}{3}\left(\frac{\partial T}{\partial r}\right)_{\text{turb}} W^{-3/2}\cos^{-1}\alpha_p \qquad (15)$$

Assuming α_p is nearly constant when $d\alpha_p/dr \to 0$, equation (13) is integrated to give $W^{3/2}\cos\alpha_p = r(\partial T/\partial r)_{\text{turb}}$ and

$$\tan\alpha_p = 1/\sqrt{3} \text{ or } \alpha_p = 30° \qquad (16)$$

This is the asymptotic value of α_p as seen from the pitch angle distribution in Figure 14.

The above calculation shows that the behavior of the heated ions is quite well predicted by a test particle approach. But in the heating process the plasma is severely affected, and plasma perturbations cannot be described by this approach.

The heating event shown in Figures 11*a* to 11*d* lasts for 20 min. After this period the plasma in the flux tube begins to recover as shown in Figure 15. The recovery is primarily through the upward expansion of the polar wind into the plasma cavity created by the transverse ion heating. The recovery seen here is somewhat similar to the polar wind expansion into a depleted flux tube previously studied by *Singh and Schunk* [1985] except for the presence of warm ions inside the cavity. Some interesting features of the recovery process are as follows. As the polar wind expands upward, its ambient properties are restored below a certain height. This height is seen to increase with a rate of about 8 km/s, which is comparable to the ion acoustic speed near the lower part of the flux tube. When $t = t_{24} = 44$ min, the recovery has occurred only up to a height $s = 15{,}000$ km, as indicated by a big open square on the density profile curve in Figure 15. As the cavity refills from the bottom, the density in the upper part of the flux tube is seen to continually decrease. This is primarily due to the relatively large velocity flow in the upper part of the cavity. The transversely heated ions move upward on top of the expanding polar wind (Figure 15*d*). Such ions in the plasma cavity are seen to progressively cool in $T_\perp$. The cooling is primarily due to heat convection. As $T_\perp$ is lowered by cooling, the flow velocity tends to relax toward the ambient polar wind flow velocity (Figure 15*b*).

It is important to note that the maximum flow velocity attained in the extended ion heating event is about 140 km/s. This velocity is ≤20% of the electron thermal velocity along the flux tube. Thus the approximation made in calculating the electric field (equation (6)) is approximately satisfied. If the evolution with heating is to be followed until later times, the electric field expression needs further improvement by relaxing the isothermal assumption of the electron temperature.

It is worth noting that the cavity on top of the expanding polar wind relaxes quite slowly. Following an extended heating event, the polar wind in the flux tube may take a few hours to relax. For example, in Figure 15 the ambient polar wind front reaches the distance $s = 52{,}000$ km (8 R_E) in about 2 hours. During this recovery time the density profile in the flux tube shows two distinct regions; below the expansion front the density profile is that of the ambient polar wind while above it the density is generally lower than the ambient polar wind density. Satellite observations do indicate such transitions in the radial density profiles in the polar region of the magnetosphere [*Persoon et al.*, 1983]. However, the reason for the density

depletion at high altitudes remains unknown. It is likely that the extended transverse ion heating at high altitudes may create the transition.

4. CONCLUSION AND DISCUSSION

The main purpose of this paper is to study the nature of plasma perturbations created by transverse ion heating in the auroral and polar region of the magnetosphere. This study is motivated by the fact that transverse ion heating is a pervasive phenomenon. The creation of the perturbations by transverse ion heating and their evolution are studied by solving a set of plasma transport equations along open flux tubes for geocentric altitudes $r \geq 9371$ km/s. Both localized and extended heating events in space have been considered. Likewise, both short- and long-duration heating events have been studied.

For localized heating, the main characteristics of the perturbation are as follows. The perturbation in the density consists of a density cavity topped by a density bump. During the early stage the plasma in the bump is that expelled from the cavity by the mirror force. The flow velocity is enhanced over the entire perturbation. The parallel temperature is lowered inside the cavity while inside the density bump it is enhanced. The reduction and increment in $T_{\parallel}$ occur approximately adiabatically ($T_{\parallel} \propto n^2$). The transversely heated ions occupy the region near the top of the cavity and the bump. However, near the leading edge of the bump there are some ions which are heated only in $T_{\parallel}$ but not in $T_{\perp}$. This is attributed to the electrostatic snowplow effect. This effect is enhanced when the electric field near the leading edge is enhanced, for example, by enhanced electron temperature. As long as the heating lasts, the lower end of the perturbation remains anchored to the lower end of the heating region while the upper end of the perturbation moves upward. After the heating ends, the entire perturbation rides on top of the upward expanding polar wind.

When the perturbations are relatively weak, produced by a relatively low transverse heating rate, the density and velocity profiles in the perturbations do not show any significant steepening. However, when the heating rate is sufficiently enhanced, the density and velocity profiles show the formation of a reverse-forward shock pair. The forward shock forms near the leading edge (top) of the density bump. It evolves through the steepening of a relatively large amplitude perturbation in the density. The reverse shock forms near the trailing edge of the density bump.

The interesting feature of the electric field distribution associated with the plasma perturbation is that the fields appear as localized pulses, both pointing upward (near F) and downward (near R). These pulses propagate upward with the density perturbation. The magnitude of the fields increases with the electron temperature. The transversely heated ions occur near R where the downward electric field causes a downward force on them. Such electric forces are comparable to the mirror force on the ions. It is shown that the reverse shock forms when the downward electric force exceeds the mirror force forming a "sawtooth" in the velocity profile.

When the heating is impulsive in both time and space, the electric field distribution eventually evolves into a unipolar upward pointing electric field near the leading edge. Such fields

appear as weak double layers, such as are observed in the auroral plasma at altitudes near 1 R_E [*Temerin et al.*, 1982]. However, it must be pointed out that if there is any connection between such observed double layers and the electric field produced by the impulsive ion heating, it remains to be explored. The observed electric fields have spatial scale lengths of a few tens of Debye lengths (~100 m). In contrast to this, in the calculations presented here we have resolved distances of the order of 60 km, which is the minimum intergrid spacing used in our calculations. For the purpose of a rigorous comparison, we need calculations which can resolve distances up to ~10 m. On the other hand, observationally it is essential that electric fields be correlated with perturbations in the plasma density. Nevertheless, present calculations show that perpendicular heating generates parallel electric fields. It is worth noting that electric field measurements may be one way of verifying the presence of plasma perturbations created by transverse ion heating.

The nature of the plasma perturbations produced by heating occurring over an extended region is found to be different from that produced by localized heating. The dominant feature of the density perturbation produced by extended ion heating is the formation of a cavity expanding ever upward as long as the heating lasts. Inside the cavity and above it the perpendicular temperature and the flow velocity are enhanced. As expected, the parallel temperature is reduced inside the cavity, and it is slightly enhanced above the cavity because of the enhanced density. Inside the cavity the profiles of density, velocity, and parallel and perpendicular temperatures reach a quasi-steady state and remain unchanged as long as the heating lasts. This steady state is achieved when the mirror force is balanced by the rate of charge of momentum due to the velocity gradients. Since the flows are highly supersonic, the thermal effects on the flow are found to be insignificant. Inside the cavity the ion motion is found to be governed by the test particle motion. The pitch angle distribution is found to reach an asymptotic value of 30° at large geocentric distances as theoretically predicted by a test particle approach [*Singh and Hwang*, 1987]. This shows that the motion of transversely heated ions can be described by a test particle approach. But it is important to note that in the process of creating the transversely heated ions the plasma is strongly perturbed and the perturbations are beyond the scope of such an approach.

The calculations presented here are based on the assumption that heating results in a bi-Maxwellian distribution and the entire ion population is affected. Such bulk heating has been observed from DE 1 [*Moore et al.*, 1985]. In situations where resonant ion heating affects only a fraction of ions, resulting in a complex velocity distribution function, the results presented can be of only limited validity. However, a rigorous treatment of resonant ion heating requires a kinetic model. It should be mentioned that when the transverse heating occurs over a broad range of energy, its evolution under the action of the mirror force gives rise to conics in the velocity distribution function. When such conical distributions evolve with increasing altitude, their parallel velocity spread increases. If this happens, the reduction of parallel temperature in the plasma cavity may be limited. This problem is difficult to treat using a fluid model for the plasma.

However, a 16-moment description of the hydrodynamic equations [*Barakat and Schunk*, 1982] shows that the parallel temperature couples to the perpendicular temperature through a heat flow term given by $2q_\perp A^{-1}\,\partial A/\partial s$ [e.g., *Ganguli and Palmadesso*, 1987]. The nature of localized heating indicates that $T_\perp$ has relatively large gradients near both bottom and top edges of the region in which transversely heated ions exist (see Figure 3). The effect of heat flows across such gradients on the parallel temperature can be estimated by a dimensional analysis of the equation $V_i dT_\parallel/ds \sim 2q_\perp A^{-1}\,\partial A/\partial s$, giving

$$\Delta T_\parallel \sim \frac{V_{th}}{V_i}\,\eta\,\epsilon\,\frac{6\Delta s}{R}\,T_\perp \qquad (17)$$

where the heat flow parameters (η and ϵ) are defined in connection with equation (5), V_i is the flow velocity, V_{th} is the thermal velocity given by $(kT_\parallel/m_i)^{1/2}$, ΔS is the spatial scale length over which $T_\perp$ varies, and R is the geocentric distance.

For the sake of concreteness, let us discuss (17) in view of the heating event shown in Figure 3. Near the lower edge of the region of transversely heated ions the temperature gradient in $T_\perp$ is upward, giving a downward heat flow $q_\perp$ which implies $\epsilon = -1$. Thus the coupling of $T_\parallel$ with $T_\perp$ through heat flow produces an additional cooling of ions inside the plasma cavity. This cooling can be physically reconciled as follows. The ions carrying thermal ($nkT_\perp$) energy downward are acted on by the upward mirror force, and thereby the spread in their parallel velocity is reduced.

Near the upper edge of the region of transversely heated ions the heat flow $q_\perp$ is upward, implying $\epsilon = +1$ and $\Delta T_\parallel > 0$. Therefore the coupling between $T_\parallel$ and $T_\perp$ near the upper edge yields an enhancement in $T_\parallel$. This agrees with the common sense that as the ions carry heat ($nkT_\perp$) upward, their parallel velocity spread increases through the action of the mirror force. In hydrodynamic models this increase in the velocity spread implies enhancement in the parallel temperature. The magnitude of this enhancement can be assessed from (17); at $t = t_4$ in Figure 3 the estimates for the various parameters appearing in this equation are $V_i \sim 50$ km/s, $V_{th} \sim 10$ km/s, $\Delta s \sim 500$ km, $R \sim 10{,}000$ km, and $T_\perp \sim 20$ eV, giving $\Delta T_\parallel \sim 1.2\eta$ eV.

Depending on the η (<1) factor, $\Delta T_\parallel$ due to the coupling between $T_\parallel$ and $T_\perp$ through the heat flow $q_\perp$ is less than the enhancement in $T_\parallel$ due to the compression of the plasma in the density enhancement. Thus the coupling between $T_\parallel$ and $T_\perp$ through perpendicular heat flow is not a dominating factor for the parameters of the heating events considered in this paper. However, it must be pointed out that in heating events producing much more energetic ions, $\Delta T_\parallel$ due to $T_\parallel$-$T_\perp$ coupling through the perpendicular heat flow can be significant, and then it cannot be ignored in the model. In the present paper we have dealt with heating events producing $T_\perp$ only up to a few tens of electron volts, for which it appears that our hydrodynamic model is adequate.

The density depletion in the cavity created by transverse ion heating is found to be more than an order of magnitude below the density of the ambient polar wind. The minimum density in the cavity is found to be ≤ 1 cm^{-3}. *Persoon et al.* [1988] have reported such low densities in the fine structures of the auroral

plasma cavity. If numerous heating spots occur randomly distributed in time and over the auroral region, the combined effect of such heating will be the creation of an extended cavity like the auroral plasma cavity observed from satellites [*Calvert*, 1981; *Persoon et al.*, 1988]. The combined effect of numerous heating spots aligned over the field lines is likely to be similar to that of extended heating.

Persoon et al. [1983] have reported basic transitions at geocentric altitudes of 1.16 R_E and 1.55 R_E in the radial distribution of the plasma density in the polar cap region. The lower-altitude transition is attributed to the transition from collisional to noncollisional flow. The transport process leading to the higher-altitude transition is not well understood. It is quite likely that low-level transverse heating extending in both time and space may be a mechanism for such a transition. We point out that the formation of cavities by ion heating may facilitate the outflow of the heavy ionospheric ions due to the enhanced parallel electric fields near the lower regions of the cavities. This is especially true if the heating and the cavity formation extend down to altitudes of ≤3000 km [*Singh et al.*, 1989].

It must be pointed out that there are numerous observations of transversely heated ions (see, for example, review by *Klumpar* [1986]). However, there is almost a total lack of any systematic observational study of how the process of transverse ion heating modifies the ambient plasma distribution in the magnetosphere. In the literature it is occasionally mentioned that ion conics are somehow correlated with severe plasma depletions [*Klumpar*, 1979, 1981]. In this paper it is shown that plasma depletions are one of several consequences of transverse ion heating whether the heating is localized or extended. Other consequences, such as the density enhancement, generation of localized parallel electric fields, and parallel heating in front of the transversely heated ions, remain to be examined observationally.

Acknowledgments. This work was supported by NASA grant NAGW-25732 made to The University of Alabama in Huntsville.

The Editor thanks H. G. Mitchell and another referee for their assistance in evaluating this paper.

REFERENCES

Ashour-Abdalla, M., and H. Okuda, Transverse acceleration of ions on auroral field lines, in *Energetic Ion Composition in the Earth's Magnetosphere*, edited by R. G. Johnson, pp. 43-72, Terra Scientific, Tokyo, 1983.

Barakat, A. R., and R. W. Schunk, Transport equations for multicomponent anisotropic space plasmas: A review, *Plasma Phys.*, *24*, 389, 1982.

Boris, J. P., and D. L. Book, Solution of continuity equations by the method of flux-corrected transport, *Methods Comput. Phys. 16*, 85, 1976.

Calvert, W., The auroral plasma cavity, *Geophys. Res. Lett.*, *8*, 919, 1981.

Chang, T., G. B. Crew, N. Hershkowitz, J. R. Jasperse, J. M. Retterer, and J. D. Winningham, Transverse acceleration of oxygen ions by electromagnetic ion cyclotron resonance with broadband left-hand polarized waves, *Geophys. Res. Lett.*, *13*, 636, 1986.

Ganguli, S. B., and P. J. Palmadesso, Plasma transport in the auroral

current region, *J. Geophys. Res., 92*, 8673, 1987.

Gombosi, T. I., and T. L. Killeen, Effects of thermospheric motions on the polar wind, *J. Geophys. Res., 92*, 4725, 1987.

Holzer, T. E., J. A. Fedder, and P. M. Banks, An expanding ion-exosphere, *J. Geophys. Res., 76*, 2455, 1971.

Horwitz, J. L., C. R. Baugher, C. R. Chappell, E. G. Shelley, and D. T. Young, Conical pitch angle distributions of very low-energy ion fluxes observed by ISEE 1, *J. Geophys. Res., 87*, 2311, 1982.

Hundhausen, A. J., Nonlinear model of high-speed solar wind streams, *J. Geophys. Res., 78*, 1528, 1973.

Kintner, P. M., M. C. Kelley, R. D. Sharp, A. G. Ghielmetti, M. Temerin, C. Cattell, P. F. Mizera, and J. F. Fennell, Simultaneous observations of energetic (keV) upstreaming ions and electrostatic hydrogen cyclotron waves, *J. Geophys. Res., 84*, 7201, 1979.

Klumpar, D. M., Transversely accelerated ions: An ionospheric source of hot magnetospheric ions, *J. Geophys. Res., 84*, 4229, 1979.

Klumpar, D. M., Transversely accelerated ions in auroral arcs, in *Physics of Auroral Arc Formation, Geophys. Monogr. Ser.*, vol. 25, edited by S. I. Akasofu and J. R. Kan, p. 122, AGU, Washington, D. C., 1981.

Klumpar, D. M., A digest and comprehensive bibliography on transverse auroral ion acceleration, in *Ion Acceleration in the Magnetosphere and Ionosphere, Geophys. Monogr. Ser.*, vol. 385 edited by T. Chang, p. 389, AGU, Washington, D. C., 1986.

Liepmann, H. W., and A. Roshko, *Elements of Gas Dynamics*, John Wiley, New York, 1957.

Manheimer, W. M., Energy flux limitations by ion acoustic turbulence in laser fusion schemes, *Phys. Fluids, 20*, 265, 1977.

Mason, R. J., Computer simulations of ion-acoustic shocks: The diaphragm problem, *Phys. Fluids, 14*, 1943, 1971.

Metzler, N., S. Cuperman, M. Dryer, and P. Rosenau, A time-dependent two-fluid model with thermal conduction for the solar wind, *Astrophys. J., 231*, 960, 1979.

Mitchell, H. G., Jr., and P. J. Palmadesso, A dynamic model for the auroral field line plasma in the presence of field-aligned current, *J. Geophys. Res., 88*, 2131, 1983.

Moore, T. E., C. R. Chappell, M. Lockwood, and J. H. Waite, Jr., Superthermal ion signatures of auroral acceleration processes, *J. Geophys. Res., 90*, 1611, 1985.

Palmadesso, P. J., S. B. Ganguli, and H. G. Mitchell, Jr., Multi-component fluid simulations of transport processes in the auroral zones in *Modeling Magnetospheric Plasma, Geophys. Monogr. Ser.*, vol. 44, edited by T. E. Moore and J. H. Waite, Jr., p. 133, AGU, Washington, D. C., 1988.

Persoon, A. M., D. A. Gurnett, and S. D. Shawhan, Polar gap electron densities from DE 1 plasma wave observations, *J. Geophys. Res., 88*, 10,123, 1983.

Persoon, A. M., D. A. Gurnett, W. K. Peterson, J. H. Waite, Jr., J. L. Burch, and J. L. Green, Electron density depletions in the nightside auroral zone, *J. Geophys. Res., 93*, 1871, 1988.

Schunk, R. W., and E. P. Szuszczewicz, Early-time plasma expansion characteristics of ionized clouds in the ionosphere, *J. Geophys. Res., 93*, 12,901, 1988.

Singh, N. and K. S. Hwang, Perpendicular ion heating effects on the refilling of the outer plasmasphere, *J. Geophys. Res., 92*, 13,513, 1987.

Singh, N., and R. W. Schunk, Numerical simulation of counter-streaming plasmas and their relevance to interhemisphere flows, *J. Geophys. Res., 88*, 7867, 1983.

current region, *J. Geophys. Res.*, *92*, 8673, 1987.

Gombosi, T. I., and T. L. Killeen, Effects of thermospheric motions on the polar wind, *J. Geophys. Res.*, *92*, 4725, 1987.

Holzer, T. E., J. A. Fedder, and P. M. Banks, An expanding ion-exosphere, *J. Geophys. Res.*, *76*, 2455, 1971.

Horwitz, J. L., C. R. Baugher, C. R. Chappell, E. G. Shelley, and D. T. Young, Conical pitch angle distributions of very low-energy ion fluxes observed by ISEE 1, *J. Geophys. Res.*, *87*, 2311, 1982.

Hundhausen, A. J., Nonlinear model of high-speed solar wind streams, *J. Geophys. Res.*, *78*, 1528, 1973.

Kintner, P. M., M. C. Kelley, R. D. Sharp, A. G. Ghielmetti, M. Temerin, C. Cattell, P. F. Mizera, and J. F. Fennell, Simultaneous observations of energetic (keV) upstreaming ions and electrostatic hydrogen cyclotron waves, *J. Geophys. Res.*, *84*, 7201, 1979.

Klumpar, D. M., Transversely accelerated ions: An ionospheric source of hot magnetospheric ions, *J. Geophys. Res.*, *84*, 4229, 1979.

Klumpar, D. M., Transversely accelerated ions in auroral arcs, in *Physics of Auroral Arc Formation*, *Geophys. Monogr. Ser.*, vol. 25, edited by S. I. Akasofu and J. R. Kan, p. 122, AGU, Washington, D. C., 1981.

Klumpar, D. M., A digest and comprehensive bibliography on transverse auroral ion acceleration, in *Ion Acceleration in the Magnetosphere and Ionosphere*, *Geophys. Monogr. Ser.*, vol. 385 edited by T. Chang, p. 389, AGU, Washington, D. C., 1986.

Liepmann, H. W., and A. Roshko, *Elements of Gas Dynamics*, John Wiley, New York, 1957.

Manheimer, W. M., Energy flux limitations by ion acoustic turbulence in laser fusion schemes, *Phys. Fluids*, *20*, 265, 1977.

Mason, R. J., Computer simulations of ion-acoustic shocks: The diaphragm problem, *Phys. Fluids*, *14*, 1943, 1971.

Metzler, N., S. Cuperman, M. Dryer, and P. Rosenau, A time-dependent two-fluid model with thermal conduction for the solar wind, *Astrophys. J.*, *231*, 960, 1979.

Mitchell, H. G., Jr., and P. J. Palmadesso, A dynamic model for the auroral field line plasma in the presence of field-aligned current, *J. Geophys. Res.*, *88*, 2131, 1983.

Moore, T. E., C. R. Chappell, M. Lockwood, and J. H. Waite, Jr., Superthermal ion signatures of auroral acceleration processes, *J. Geophys. Res.*, *90*, 1611, 1985.

Palmadesso, P. J., S. B. Ganguli, and H. G. Mitchell, Jr., Multi-component fluid simulations of transport processes in the auroral zones in *Modeling Magnetospheric Plasma*, *Geophys. Monogr. Ser.*, vol. 44, edited by T. E. Moore and J. H. Waite, Jr., p. 133, AGU, Washington, D. C., 1988.

Persoon, A. M., D. A. Gurnett, and S. D. Shawhan, Polar gap electron densities from DE 1 plasma wave observations, *J. Geophys. Res.*, *88*, 10,123, 1983.

Persoon, A. M., D. A. Gurnett, W. K. Peterson, J. H. Waite, Jr., J. L. Burch, and J. L. Green, Electron density depletions in the nightside auroral zone, *J. Geophys. Res.*, *93*, 1871, 1988.

Schunk, R. W., and E. P. Szuszczewicz, Early-time plasma expansion characteristics of ionized clouds in the ionosphere, *J. Geophys. Res.*, *93*, 12,901, 1988.

Singh, N. and K. S. Hwang, Perpendicular ion heating effects on the refilling of the outer plasmasphere, *J. Geophys. Res.*, *92*, 13,513, 1987.

Singh, N., and R. W. Schunk, Numerical simulation of counter-streaming plasmas and their relevance to interhemisphere flows, *J. Geophys. Res.*, *88*, 7867, 1983.

Singh, N., and R. W. Schunk, Energization of ions in the auroral plasma by broadband waves: Generation of ion conics, *J. Geophys. Res., 89*, 5538, 1984.

Singh, N., and R. W. Schunk, Temporal behavior of density perturbations in the polar wind, *J. Geophys. Res., 90*, 6487, 1985.

Singh, N., K. S. Hwang, D. G. Torr, and P. Richards, Temporal features of the outflow of heavy ionospheric ions in response to a high altitude plasma cavity, *Geophys. Res. Lett., 16*, 29, 1989.

Temerin, M., Evidence of a large bulk ion conic heating region, *Geophys. Res. Lett., 13*, 1059, 1986.

Temerin, M., K. Cerny, W. Lottko, and F. S. Mozer, Observations of double layers and solitary waves in the auroral plasma, *Phys. Rev. Lett., 48*, 1175, 1982.

Tanenbaum, B. S., *Plasma Physics*, McGraw-Hill, New York, 1967.

Tidman, D. A., and N. A. Krall, *Shock Waves in Collisionless Plasmas*, Wiley-Interscience, New York, 1971.

N. Singh, University of Alabama, Department of Electrical and Computer Engineering, EB-267, Huntsville, AL 35899.

(Received November 28, 1990;
revised August 5, 1991;
accepted August 8, 1991.)

Paper number 91JA02436.
0148-0227/92/91JA-02436$05.00

SINGH: TRANSVERSE ION HEATING AND PLASMA PERTURBATIONS

SINGH: TRANSVERSE ION HEATING AND PLASMA PERTURBATIONS

SINGH: TRANSVERSE ION HEATING AND PLASMA PERTURBATIONS

SINGH: TRANSVERSE ION HEATING AND PLASMA PERTURBATIONS

SINGH: TRANSVERSE ION HEATING AND PLASMA PERTURBATIONS

SINGH: TRANSVERSE ION HEATING AND PLASMA PERTURBATIONS

SINGH: TRANSVERSE ION HEATING AND PLASMA PERTURBATIONS

SINGH: TRANSVERSE ION HEATING AND PLASMA PERTURBATIONS

SINGH: TRANSVERSE ION HEATING AND PLASMA PERTURBATIONS

SINGH: TRANSVERSE ION HEATING AND PLASMA PERTURBATIONS

SINGH: TRANSVERSE ION HEATING AND PLASMA PERTURBATIONS

SINGH: TRANSVERSE ION HEATING AND PLASMA PERTURBATIONS

SINGH: TRANSVERSE ION HEATING AND PLASMA PERTURBATIONS

SINGH: TRANSVERSE ION HEATING AND PLASMA PERTURBATIONS

SINGH: TRANSVERSE ION HEATING AND PLASMA PERTURBATIONS

SINGH: TRANSVERSE ION HEATING AND PLASMA PERTURBATIONS
SINGH: TRANSVERSE ION HEATING AND PLASMA PERTURBATIONS
SINGH: TRANSVERSE ION HEATING AND PLASMA PERTURBATIONS
SINGH: TRANSVERSE ION HEATING AND PLASMA PERTURBATIONS
SINGH: TRANSVERSE ION HEATING AND PLASMA PERTURBATIONS
SINGH: TRANSVERSE ION HEATING AND PLASMA PERTURBATIONS
SINGH: TRANSVERSE ION HEATING AND PLASMA PERTURBATIONS
SINGH: TRANSVERSE ION HEATING AND PLASMA PERTURBATIONS
SINGH: TRANSVERSE ION HEATING AND PLASMA PERTURBATIONS
SINGH: TRANSVERSE ION HEATING AND PLASMA PERTURBATIONS
SINGH: TRANSVERSE ION HEATING AND PLASMA PERTURBATIONS
SINGH: TRANSVERSE ION HEATING AND PLASMA PERTURBATIONS
SINGH: TRANSVERSE ION HEATING AND PLASMA PERTURBATIONS
SINGH: TRANSVERSE ION HEATING AND PLASMA PERTURBATIONS
SINGH: TRANSVERSE ION HEATING AND PLASMA PERTURBATIONS
SINGH: TRANSVERSE ION HEATING AND PLASMA PERTURBATIONS
SINGH: TRANSVERSE ION HEATING AND PLASMA PERTURBATIONS
SINGH: TRANSVERSE ION HEATING AND PLASMA PERTURBATIONS
SINGH: TRANSVERSE ION HEATING AND PLASMA PERTURBATIONS
SINGH: TRANSVERSE ION HEATING AND PLASMA PERTURBATIONS
SINGH: TRANSVERSE ION HEATING AND PLASMA PERTURBATIONS
SINGH: TRANSVERSE ION HEATING AND PLASMA PERTURBATIONS
SINGH: TRANSVERSE ION HEATING AND PLASMA PERTURBATIONS
SINGH: TRANSVERSE ION HEATING AND PLASMA PERTURBATIONS
SINGH: TRANSVERSE ION HEATING AND PLASMA PERTURBATIONS
SINGH: TRANSVERSE ION HEATING AND PLASMA PERTURBATIONS
SINGH: TRANSVERSE ION HEATING AND PLASMA PERTURBATIONS
SINGH: TRANSVERSE ION HEATING AND PLASMA PERTURBATIONS
SINGH: TRANSVERSE ION HEATING AND PLASMA PERTURBATIONS
SINGH: TRANSVERSE ION HEATING AND PLASMA PERTURBATIONS

SINGH: TRANSVERSE ION HEATING AND PLASMA PERTURBATIONS

SINGH: TRANSVERSE ION HEATING AND PLASMA PERTURBATIONS

SINGH: TRANSVERSE ION HEATING AND PLASMA PERTURBATIONS

SINGH: TRANSVERSE ION HEATING AND PLASMA PERTURBATIONS

SINGH: TRANSVERSE ION HEATING AND PLASMA PERTURBATIONS

SINGH: TRANSVERSE ION HEATING AND PLASMA PERTURBATIONS

SINGH: TRANSVERSE ION HEATING AND PLASMA PERTURBATIONS

SINGH: TRANSVERSE ION HEATING AND PLASMA PERTURBATIONS

SINGH: TRANSVERSE ION HEATING AND PLASMA PERTURBATIONS

Fig. 1. Geometry of the calculation. The lower and upper boundaries of the calculation region are at geocentric distances $r=r_o=9371$ km and $r=r_{max}=93{,}371$ km. The distance from the lower boundary is s.

Fig. 2. Plasma perturbations in response to a relatively weak heating rate of 0.24 eV/s: (*a*) density, (*b*) flow velocity, (*c*) parallel temperature, and (*d*) perpendicular temperature. The curves shown in these panels are at times $t_n = 0.922 \times n$ for $n = 1, 2, 4$, and 6. Electron temperature T_e is 1 eV; heating time Δt_h is 1.844 min and heating region size Δs_h is 210 km.

Fig. 3. Same as Figure 2, but for a relatively strong heating rate of 2.4 eV/s.

Fig. 4. Electric field distribution at (*a*) $t = t_1$, (*b*) $t = t_2$, (*c*) $t = t_4$, and (*d*) $t = t_6$. The solid curves are the electric field calculated solely from the gradients in the density profile while the circles on the curves are the sum of the contributions from $\partial n/\partial s$, $\partial V/\partial r$, and $\partial V/\partial t$ in equation (6). Note that the electric field is quite accurately described by the density gradients alone. Parameters for this figure are the same as in Figure 3.

Fig. 5. Comparison between the electric fields from Figure 4 with the mirror force F_m. The dashed curves show F_m/e.

Fig. 6. Same as Figure 3, except for $\Delta t_h = 0.1844$ min and heating rate of 24 eV/s.

Fig. 7. Comparison between plasma perturbations for $\eta = 0.01$ (dashed curve) and $\eta = 1$ (solid curve). Left- and right-hand panels are for early ($t = t_2$) and late ($t = t_6$) times, respectively. Other parameters are the same as in Figure 3.

Fig. 8. Same as Figure 3, but for electron temperature linearly increasing with altitude from 0.3 eV at $s = 0$ to 3 eV at $s = 12{,}000$ km.

Fig. 9. Electric fields at (*a*) $t = t_1$, (*b*) $t = t_2$, (*c*) $t = t_4$, and (*d*) $t = t_6$ associated with the perturbation in Figure 8.

Fig. 10. Plasma perturbations in response to impulsive heating in both time and space ($\Delta t_h = 5$ s, $\Delta s_h = 60$ km). Electron temperature T_e is 10 eV. (*a*, *b*, *c*, and *d*) Evolution of n(s), V(s), $T_{\parallel}$(s), and $T_{\perp}$(s), respectively. (*e*, *f*, *g*, and *h*) Evolution of the electric field distribution.

Fig. 11. Plasma perturbations in response to an extended heating event: (*a*) density, (*b*) velocity, (*c*) parallel temperature, and (*d*) perpendicular temperature. Heating rate is 0.24 eV/s. The profiles shown are at times $t_n = n \times 1.844$ min, $n = 1, 3, 5, 7$, and 9. Heating terminates at $t = t_{11} = 20$ min.

Fig. 12. Comparison of flow velocities (dashed curves) obtained by integrating equation (10) with those (solid curves) given in Figure 11*b* at times (*a*) t_3, (*b*) t_5, (*c*) t_7, and (*d*) t_9. Note the good agreement between the two sets of curves inside the cavity. The top of the cavity is indicated by the arrows.

Fig. 13. Same as Figure 11*d*, but on a linear scale.

Fig. 14. Pitch angle distribution at $t = t_9$ for the extended heating shown in Figure 11.

Fig. 15. Polar wind recovery after the heating ceases at $t = t_{11}$: (*a*) density, (*b*) velocity, (*c*) parallel temperature, and (*d*) perpendicular temperature.

Fig. 1. Geometry of the calculation. The lower and upper boundaries of the calculation region are at geocentric distances $r = r_o = 9371$ km and $r = r_{max} = 93{,}371$ km. The distance from the lower boundary is s.

Fig. 2. Plasma perturbations in response to a relatively weak heating rate of 0.24 eV/s: (*a*) density, (*b*) flow velocity, (*c*) parallel temperature, and (*d*) perpendicular temperature. The curves shown in these panels are at times $t_n = 0.922 \times n$ for $n = 1$, 2, 4, and 6. Electron temperature T_e is 1 eV; heating time Δt_h is 1.844 min and heating region size Δs_h is 210 km.

Fig. 3. Same as Figure 2, but for a relatively strong heating rate of 2.4 eV/s.

Fig. 4. Electric field distribution at (*a*) $t = t_1$, (*b*) $t = t_2$, (*c*) $t = t_4$, and (*d*) $t = t_6$. The solid curves are the electric field calculated solely from the gradients in the density profile while the circles on the curves are the sum of the contributions from $\partial n/\partial s$, $\partial V/\partial r$, and $\partial V/\partial t$ in equation (6). Note that the electric field is quite accurately described by the density gradients alone. Parameters for this figure are the same as in Figure 3.

Fig. 5. Comparison between the electric fields from Figure 4 with the mirror force F_m. The dashed curves show F_m/e.

Fig. 6. Same as Figure 3, except for $\Delta t_h = 0.1844$ min and heating rate of 24 eV/s.

Fig. 7. Comparison between plasma perturbations for $\eta = 0.01$ (dashed curve) and $\eta = 1$ (solid curve). Left- and right-hand panels are for early ($t = t_2$) and late ($t = t_6$) times, respectively. Other parameters are the same as in Figure 3.

Fig. 8. Same as Figure 3, but for electron temperature linearly increasing with altitude from 0.3 eV at $s = 0$ to 3 eV at $s = 12{,}000$ km.

Fig. 9. Electric fields at (*a*) $t = t_1$, (*b*) $t = t_2$, (*c*) $t = t_4$, and (*d*) $t = t_6$ associated with the perturbation in Figure 8.

Fig. 10. Plasma perturbations in response to impulsive heating in both time and space ($\Delta t_h = 5$ s, $\Delta s_h = 60$ km). Electron temperature T_e is 10 eV. (*a*, *b*, *c*, and *d*) Evolution of n(s), V(s), $T_\parallel$(s), and $T_\perp$(s), respectively. (*e*, *f*, *g*, and *h*) Evolution of the electric field distribution.

Fig. 11. Plasma perturbations in response to an extended heating event: (*a*) density, (*b*) velocity, (*c*) parallel temperature, and (*d*) perpendicular temperature. Heating rate is 0.24 eV/s. The profiles shown are at times $t_n = n \times 1.844$ min, $n = 1$, 3, 5, 7, and 9. Heating terminates at $t = t_{11} = 20$ min.

Fig. 12. Comparison of flow velocities (dashed curves) obtained by integrating equation (10) with those (solid curves) given in Figure 11*b* at times (*a*) t_3, (*b*) t_5, (*c*) t_7, and (*d*) t_9. Note the good agreement between the two sets of curves inside the

cavity. The top of the cavity is indicated by the arrows.

Fig. 13. Same as Figure 11*d*, but on a linear scale.

Fig. 14. Pitch angle distribution at $t = t_9$ for the extended heating shown in Figure 11.

Fig. 15. Polar wind recovery after the heating ceases at $t = t_{11}$: (*a*) density, (*b*) velocity, (*c*) parallel temperature, and (*d*) perpendicular temperature.

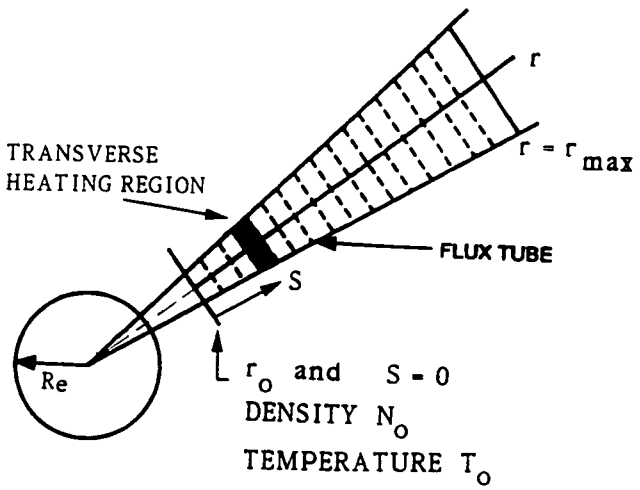
r
r = r max
TRANSVERSE
HEATING REGION
FLUX TUBE
S
Re
r o and S = 0
DENSITY N o
TEMPERATURE T o

Fig. 1

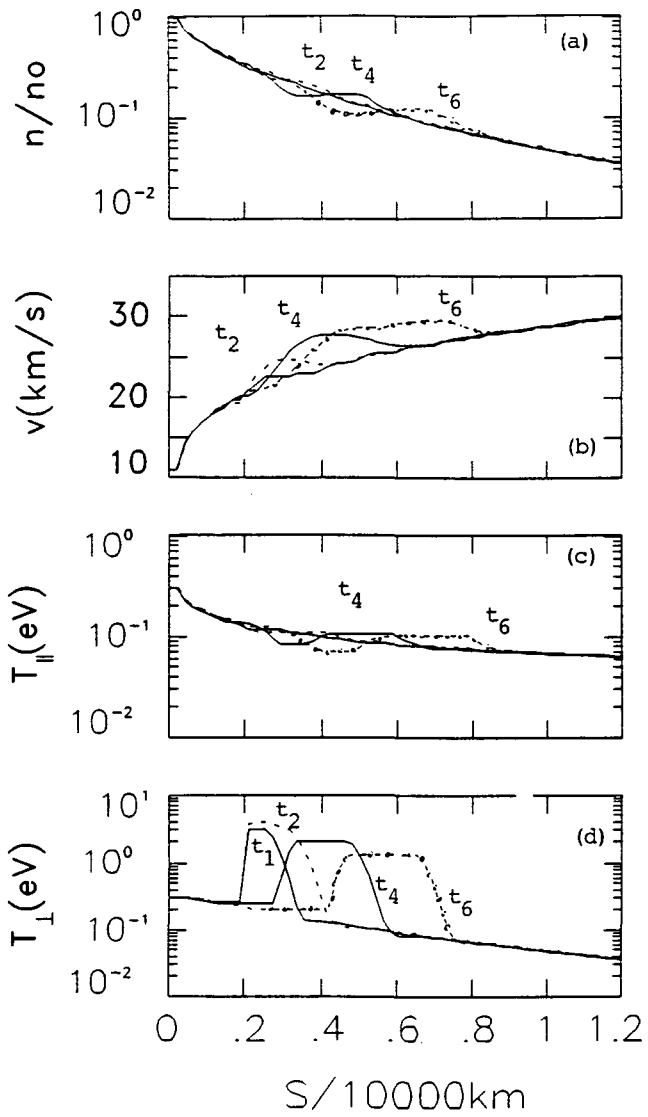
n/no
10^0
10^{-1}
10^{-2}
(a)
t_2
t_4
t_6
v(km/s)
30
20
10
(b)
t_2
t_4
t_6
$T_{\parallel}$(eV)
10^0
10^{-1}
10^{-2}
(c)
t_4
t_6
$T_{\perp}$(eV)
10^1
10^0
10^{-1}
10^{-2}
(d)
t_1
t_2
t_4
t_6
0 .2 .4 .6 .8 1 1.2
S/10000km

Fig. 2

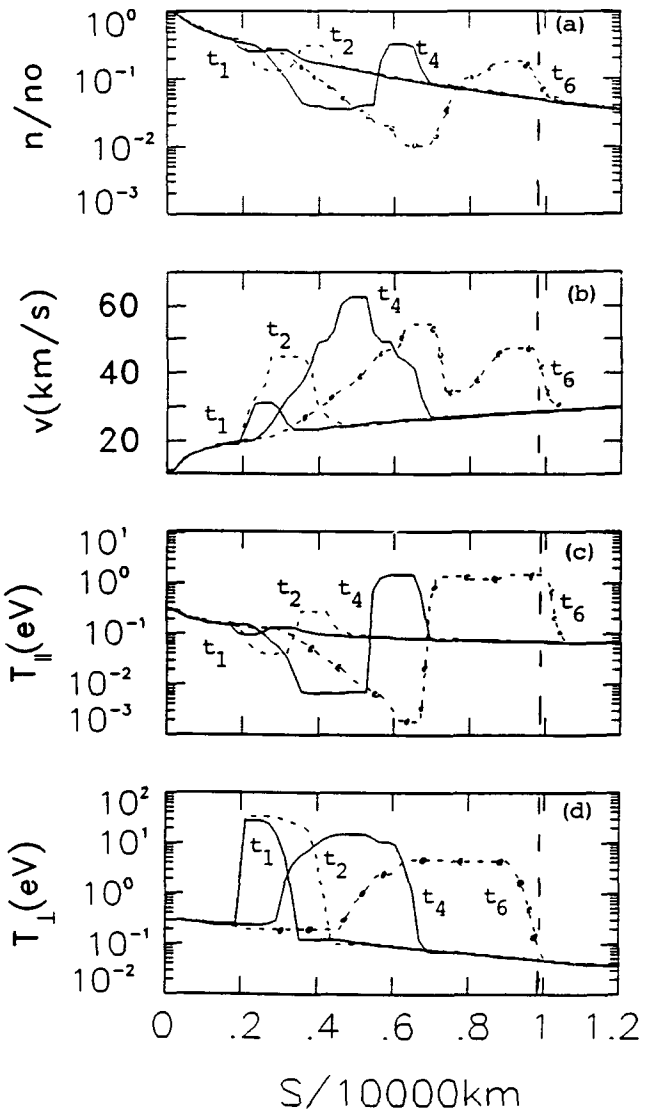
n/no
10⁰
10⁻¹
10⁻²
10⁻³
(a)
t1
t2
t4
t6
v(km/s)
60
40
20
(b)
T∥(eV)
10¹
10⁰
10⁻¹
10⁻²
10⁻³
(c)
T⊥(eV)
10²
10¹
10⁰
10⁻¹
10⁻²
(d)
0
.2
.4
.6
.8
1
1.2
S/10000km

Fig. 3

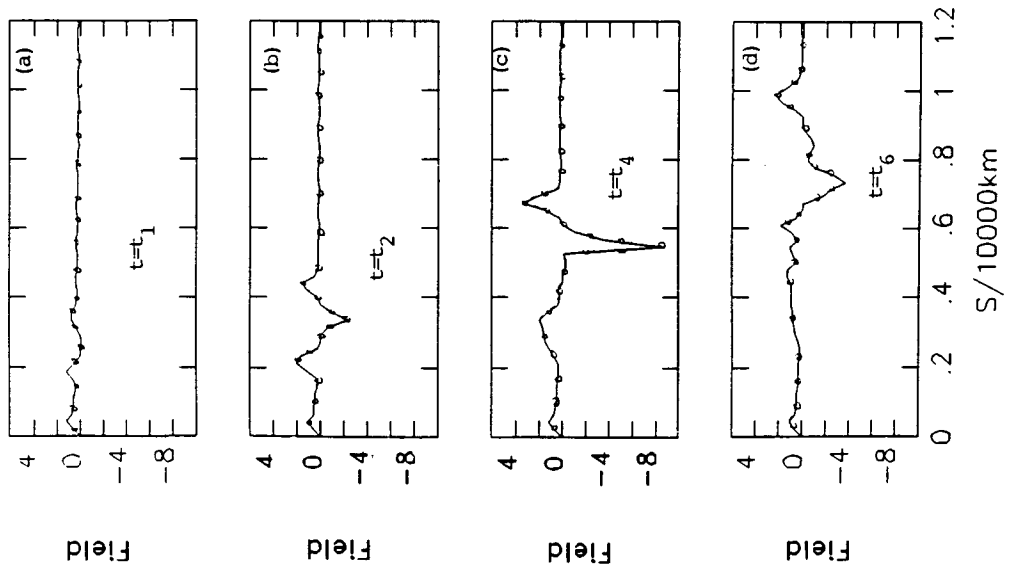

Fig. 4

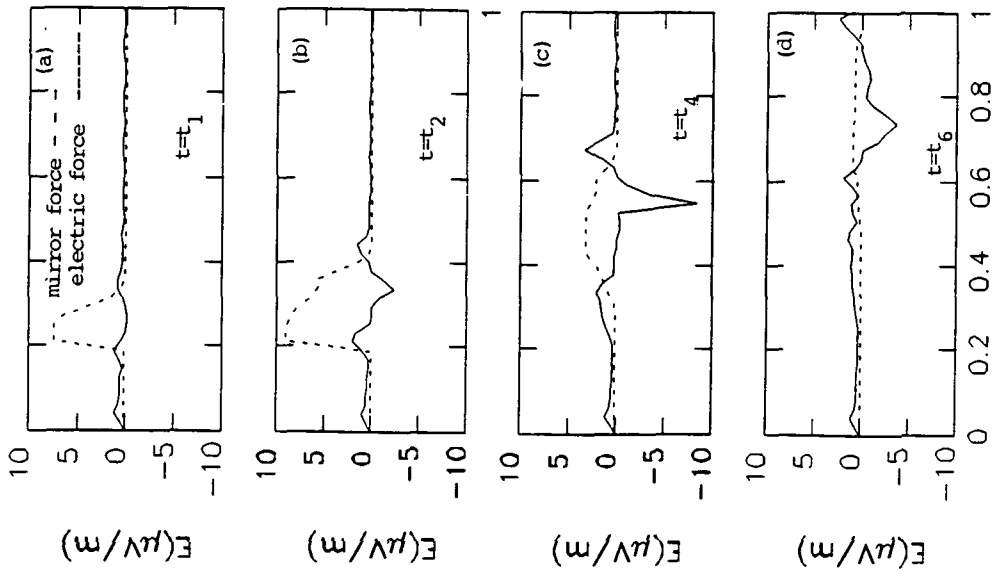
mirror force - - -
electric force ------
(a)
(b)
(c)
(d)
t=t1
t=t2
t=t4
t=t6
E(μV/m)
10
5
0
-5
-10
0
0.2
0.4
0.6
0.8
1
S/10000km

Fig. 5

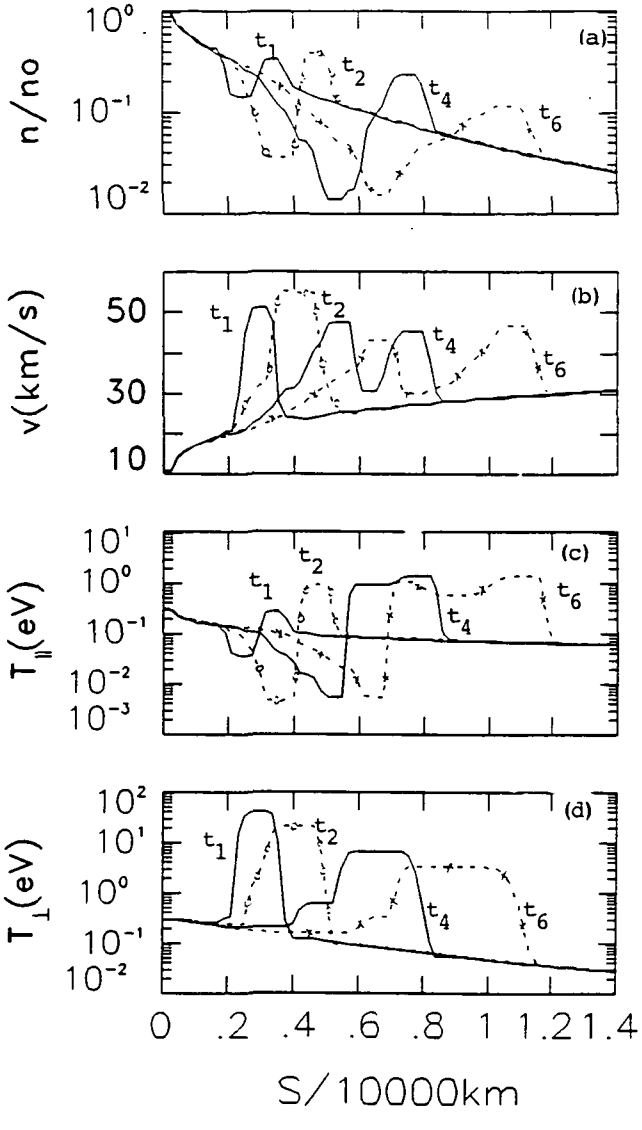
n/no
10^0
10^-1
10^-2
(a)
t1
t2
t4
t6
v(km/s)
50
30
10
(b)
T||(eV)
10^1
10^0
10^-1
10^-2
10^-3
(c)
T⊥(eV)
10^2
10^1
10^0
10^-1
10^-2
(d)
0 .2 .4 .6 .8 1 1.2 1.4
S/10000km

Fig. 6

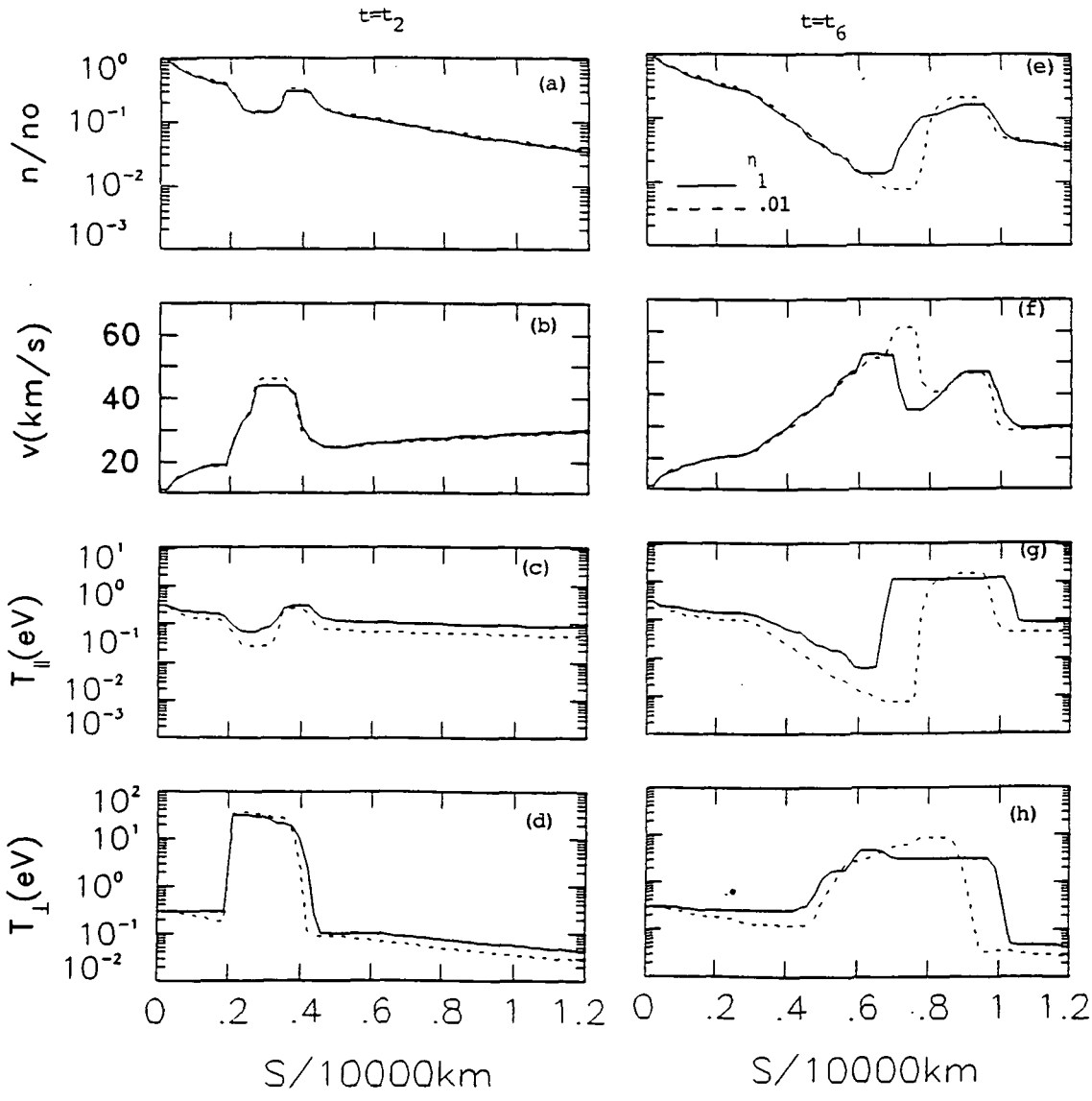
t=t2
t=t6
n/no
10^0
10^-1
10^-2
10^-3
(a)
(e)
η
1
.01
v(km/s)
60
40
20
(b)
(f)
T||(eV)
10'
10^0
10^-1
10^-2
10^-3
(c)
(g)
T⊥(eV)
10^2
10'
10^0
10^-1
10^-2
(d)
(h)
0 .2 .4 .6 .8 1 1.2
S/10000km
0 .2 .4 .6 .8 1 1.2
S/10000km

Fig. 7

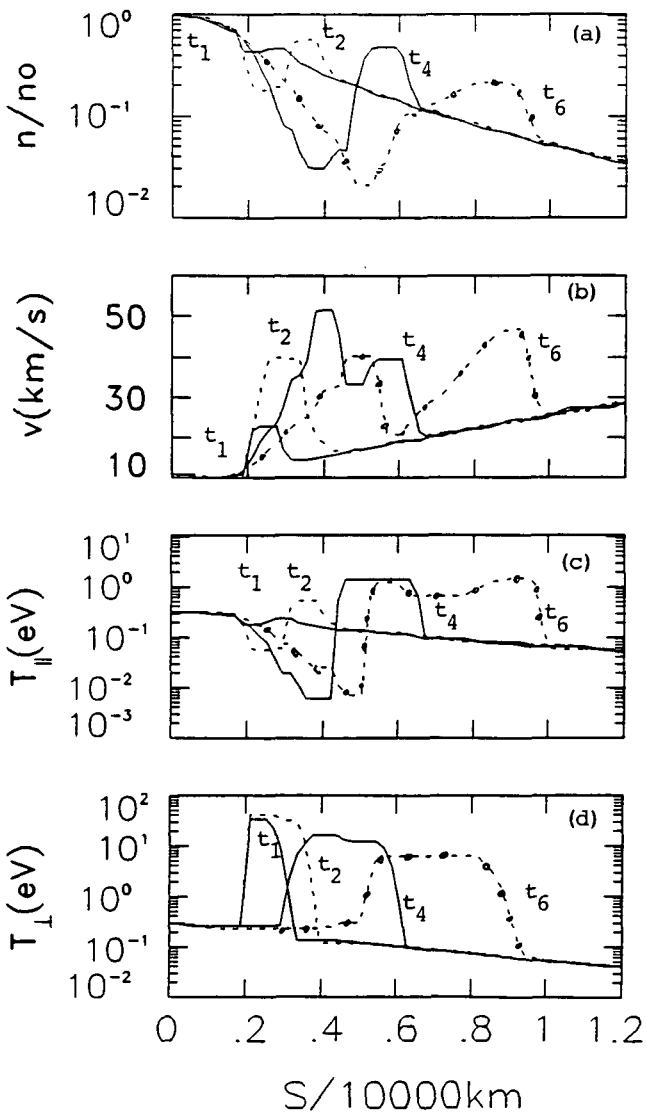
n/no
10^0
10^{-1}
10^{-2}
(a)
t_1
t_2
t_4
t_6
v(km/s)
50
30
10
(b)
$T_{\parallel}$(eV)
10^1
10^0
10^{-1}
10^{-2}
10^{-3}
(c)
$T_{\perp}$(eV)
10^2
10^1
10^0
10^{-1}
10^{-2}
(d)
0 .2 .4 .6 .8 1 1.2
S/10000km

Fig 8

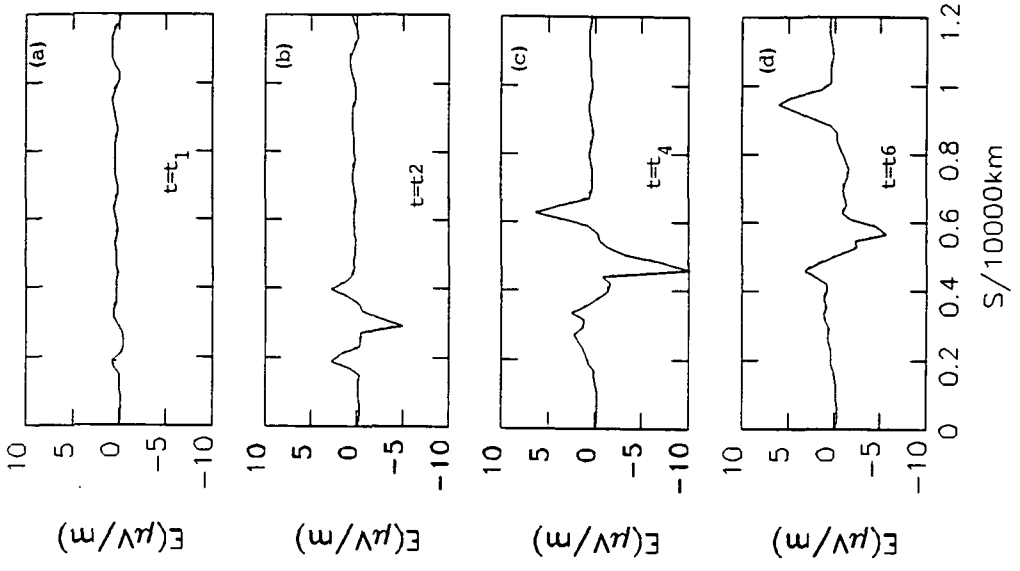

Fig. 9

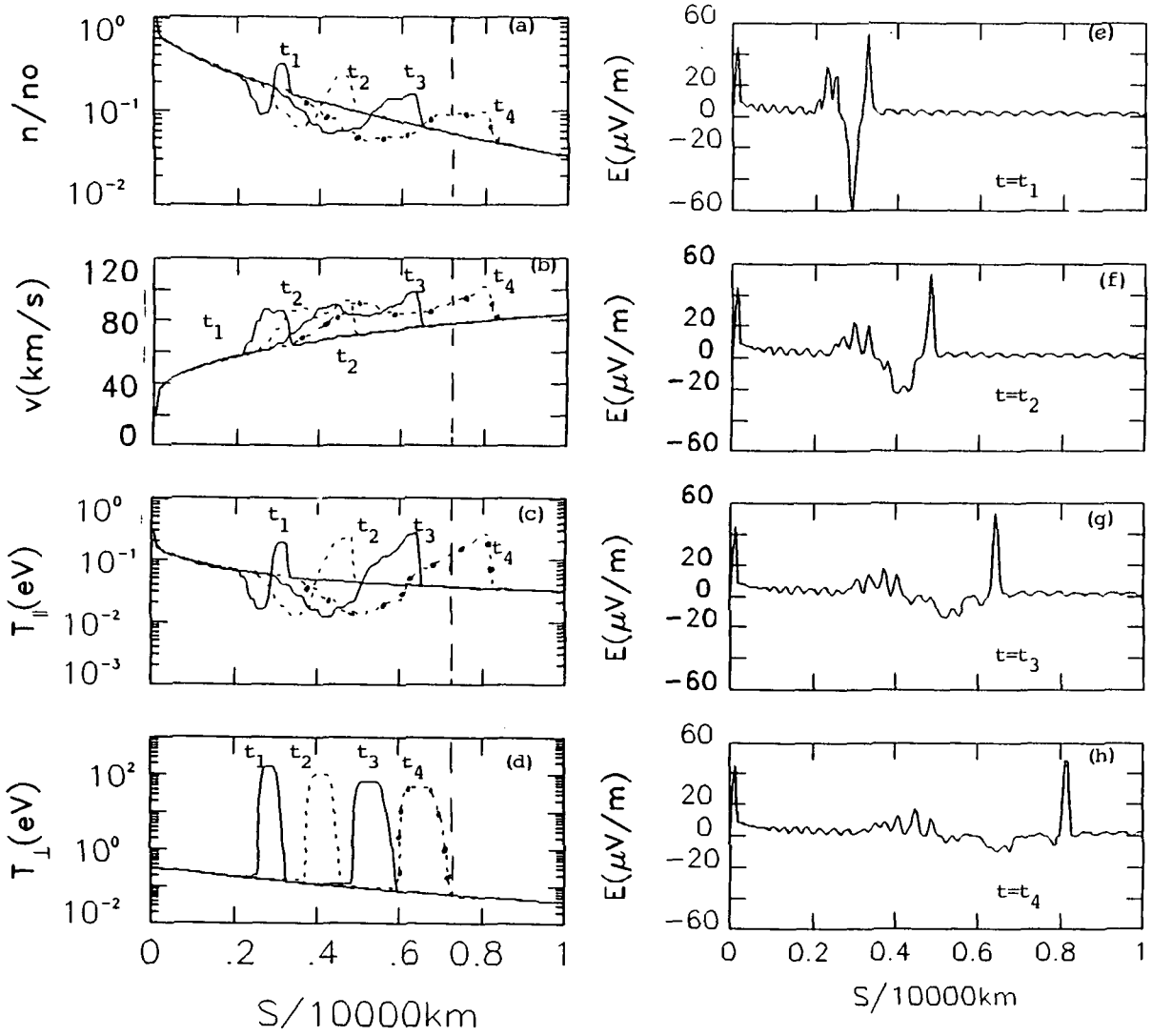
n/no
v(km/s)
T∥(eV)
T⊥(eV)
E(μV/m)
(a)
(b)
(c)
(d)
(e)
(f)
(g)
(h)
t1
t2
t3
t4
t=t1
t=t2
t=t3
t=t4
S/10000km

Fig. 10

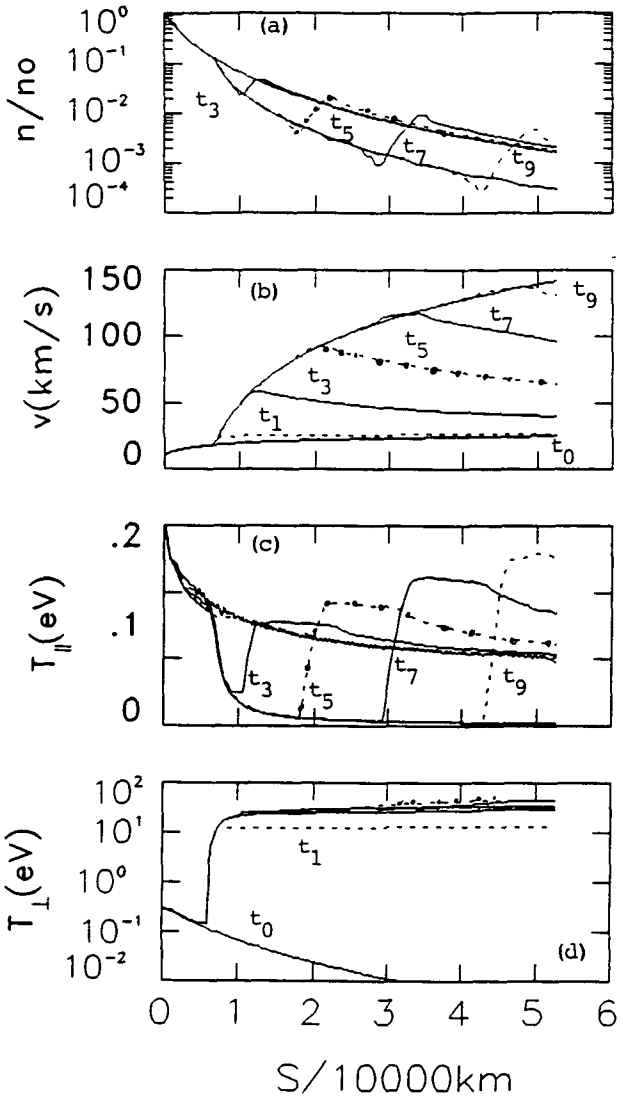
(a)
n/no
10^0
10^{-1}
10^{-2}
10^{-3}
10^{-4}
t_3
t_5
t_7
t_9
(b)
v(km/s)
150
100
50
0
t_9
t_7
t_5
t_3
t_1
t_0
(c)
$T_{\parallel}$(eV)
.2
.1
0
t_3
t_5
t_7
t_9
$T_{\perp}$(eV)
10^2
10^1
10^0
10^{-1}
10^{-2}
t_1
t_0
(d)
0 1 2 3 4 5 6
S/10000km

Fig. 11

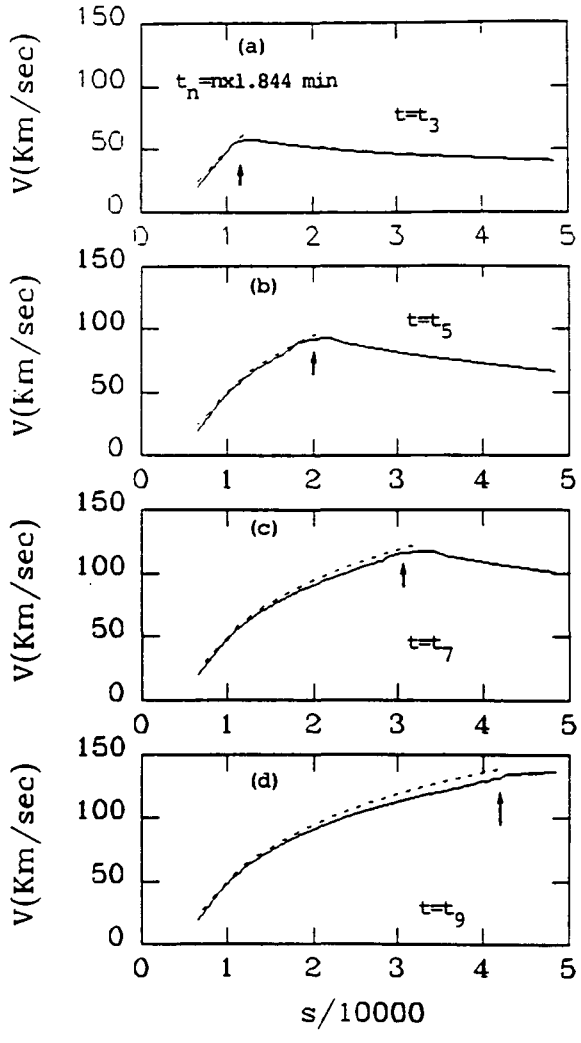
150
100
50
0
V(Km/sec)
(a)
t_n=nx1.844 min
t=t_3
(b)
t=t_5
(c)
t=t_7
(d)
t=t_9
0 1 2 3 4 5
s/10000

Fig. 12

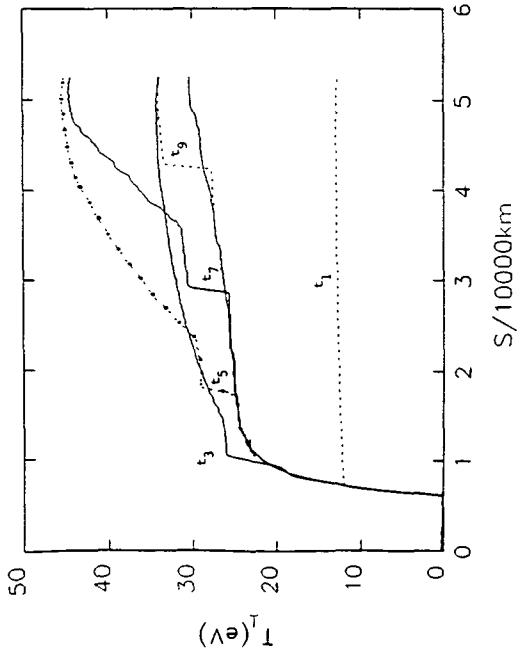

Fig. 13

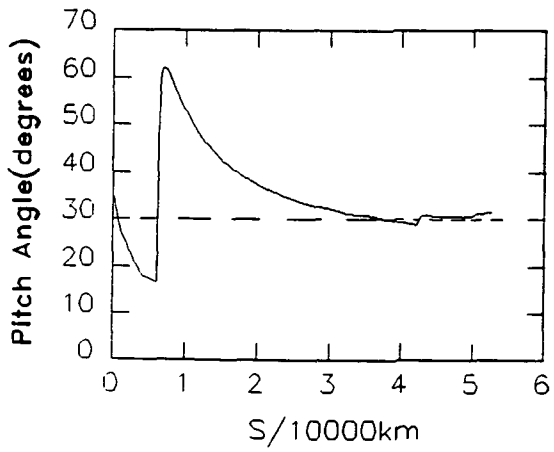

Fig. 14

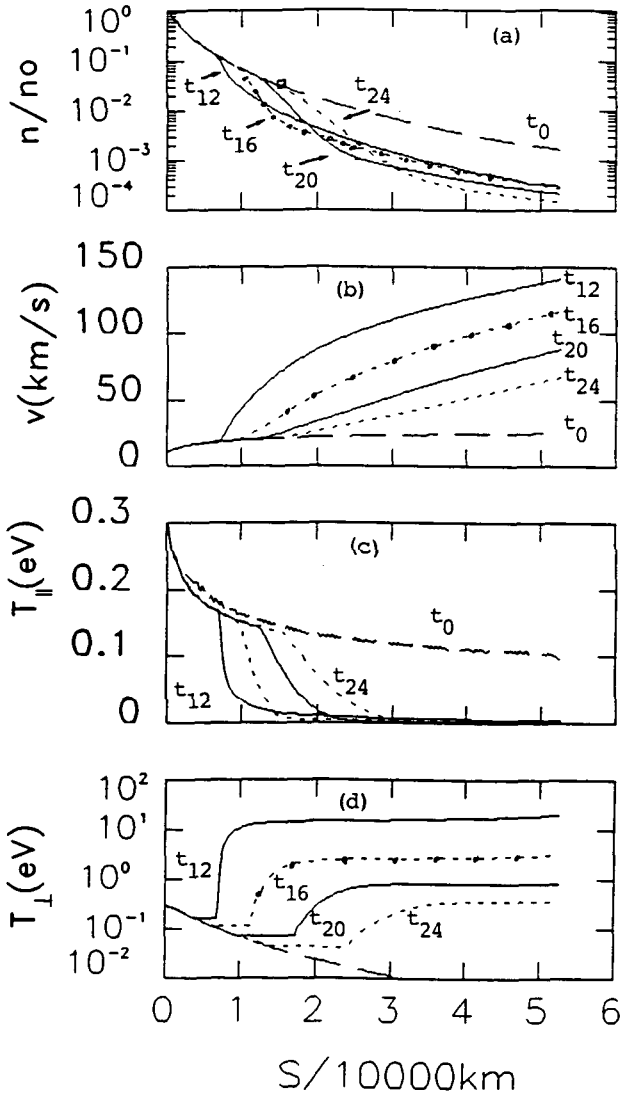
(a)
n/no
10^0
10^{-1}
10^{-2}
10^{-3}
10^{-4}
t_{12}
t_{16}
t_{20}
t_{24}
t_0
(b)
v(km/s)
150
100
50
0
t_{12}
t_{16}
t_{20}
t_{24}
t_0
(c)
$T_{\parallel}$(eV)
0.3
0.2
0.1
0
t_0
t_{24}
t_{12}
(d)
$T_{\perp}$(eV)
10^2
10^1
10^0
10^{-1}
10^{-2}
t_{12}
t_{16}
t_{20}
t_{24}
0 1 2 3 4 5 6
S/10000km

Fig. 15